

A survey of debris trails from short-period comets

William T. Reach

Spitzer Science Center/Infrared Processing and Analysis Center, MS 220-6, California
Institute of Technology, Pasadena, CA 91125

reach@ipac.caltech.edu

Michael S. Kelley

Department of Astronomy, University of Minnesota, Minneapolis, MN 55455

Mark V. Sykes

Planetary Science Institute, 1700 E Ft. Lowell, Suite 106, Planetary Science Institute,
Tucson, AZ 85719

Received _____; accepted April 2007

Manuscript Pages: 78, Tables: 3, Figures: 13

Proposed running head: Cometary Debris Trails

Editorial correspondence to:

Dr. William T. Reach

Spitzer Science Center

MS 220-6

Caltech

Pasadena, CA 91125

Phone: 626-395-8565

Fax: 626-432-7484

E-mail: reachipac.caltech.edu

We observed 34 comets using the 24 μm camera on the *Spitzer Space Telescope*. Each image contains the nucleus and covers at least 10^6 km of each comet’s orbit. Debris trails due to mm-sized or larger particles were found along the orbits of 27 comets; 4 comets had small-particle dust tails and a viewing geometry that made debris trails impossible to distinguish; and only 3 had no debris trail despite favorable observing conditions. There are now 30 Jupiter-family comets with known debris trails, of which 22 are reported in this paper for the first time. The detection rate is $> 80\%$, indicating that debris trails are a generic feature of short-period comets. By comparison to orbital calculations for particles of a range of sizes ejected over 2 yr prior to observation, we find that particles comprising 4 debris trails are typically mm-sized while the remainder of the debris trails require particles larger than this. The lower-limit masses of the debris trails are typically 10^{11} g, and the median mass loss rate is 2 kg/s. The mass-loss rate in trail particles is comparable to that inferred from OH production rates and larger than that inferred from visible-light scattering in comae.

Keywords: comets, meteors, infrared observations, interplanetary dust

1. Introduction

The composition and structure of cometary nuclei remains largely unknown. Most information about comets derives from their two best-determined observable properties: their orbits and the apparent nature of the material they eject when they approach the Sun. The nuclei themselves are very dark, offering few clues to their nature other than their size, shape, and color (Lamy et al. 2004; Weissman and Lowry 2003). Understanding cometary structure and composition is key to understanding the formation of the outer planets and the origin of the outermost layers, especially oceans and organic material, on Earth (Chyba et al. 1990; Thomas et al. 1996). Specifically, the Earth’s outermost layers and oceans are likely to have been deposited by the late bombardment of the early Earth by cometary bodies, if we define comets as those bodies on which water was in icy form at the time of initial planetesimal/cometesimal coagulation in the solar nebula (Delsemme 2000). The cause of the well-known 1908 Tunguska event (Turco et al. 1982) has been debated as an asteroidal or cometary disruption in the atmosphere (Chyba et al. 1993), but how well do we really know the difference between asteroids and comets? The cometary bodies left over from the formation of the cores of Jupiter and Saturn may have been largely scattered to the Oort cloud, while the remaining comets that formed Uranus and Neptune, as well as their (and some of Saturn’s) numerous moons, are likely residents of the present Kuiper Belt. The Kuiper Belt is the dynamical origin of the present Jupiter-family, also called ‘short-period,’ comets (Levison and Duncan 1994), whose nature we will explore in the present work.

The most significant breakthrough in understanding the physical nature of comets was the revolutionary work by Whipple (1950), in which he demonstrated that cometary orbital perturbations (beyond those that could be explained by the major planets) were caused by non-gravitational forces due to material ejected by sublimating ices heated by

the Sun during perihelion passages. The model has now advanced to include anisotropic emission from hot-spots or ‘jets’ on rotating nuclei, which are required both to provide the non-gravitational forces that change comets’ orbits from revolution to revolution as well as the fan-shaped comae (Sekanina 1979, 1988). Whipple’s model of the comet is often described as a ‘dirty snowball,’ a nickname that suggests several prevailing beliefs about cometary nature. Foremost, the nickname promotes the critical role played by icy material in powering the mass-loss that is the defining characteristic of comets. The nickname also suggests that solid material is a relatively minor constituent, and that it is in the form of small particles scattered throughout a loosely agglomerated set of ice crystals. This belief, however, is not borne out by observational studies of comets, including *in situ* studies by spacecraft (Keller et al. 2004), remote infrared observations (Sykes and Walker 1992, e.g.), and the observations presented in this paper.

Whipple himself frequently mentioned and wrote about the connection between comets and meteors. In paper II (Whipple 1951) of his classic series, he describes how solid particles are ejected from comets. An example in that paper estimates the ejection velocity of particles with 1 cm radius as 3 m s^{-1} and associates such particles with photographic meteors. The mass fraction of rock versus ice in cometary nuclei was unknown at the time of the development of Whipple’s comet model. In paper III of his series, he adopted a 20% fraction of cometary mass in the form of solid material. However, the model does not require a particularly high or low ice content in order to explain the properties of cometary orbits or mass loss.

Modern views (e.g. Prialnik et al. 2004) of comets recognize the processing and evolution of cometary material both while in the outer solar system and after capture into orbits that characterize short-period comets. The water-powered dirty snowball model could not explain why many comets are active at great distances (Meech and Svoren 2004),

or why activity is not restricted to being very close to the Sun for older comets. With the observation of significant activity in jets, the evolution of comets and their devolatilization is complicated by the details of composition and the location of active regions on a comet’s surface coupled with the orientation of the comet spin axis. Comets possessing highly volatile ices such as CO may be observed to be active at great heliocentric distances. While some comets can decrease in their activity as they approach perihelion as jets become shadowed from the Sun. This makes the detailed characterization of comet activity as a group difficult.

The current conceptual model has comets devolatilizing even while in the outer Solar System, then more rapidly upon entering a low-perihelion orbit. Sublimating gases carry away particles small enough that their drag forces exceed gravitational pull of the nucleus (Whipple 1951):

$$s < 19f_A/r^{9/4}R, \tag{1}$$

where s is the radius of the particle (cm), f_A is the fraction of the comet surface with exposed ice (taking the latent heat to be that of H₂O), r is the distance from the Sun (AU), the density of the cometary nucleus is taken to be 1 g cm⁻³, and R is the nuclear radius (km). For comets with radii of order 1 km producing dust around 1 AU from the Sun using ice covering 10% of their area, the maximum particle size is of order 2 cm. As the fine dust and ice are removed, a ‘mantle’ or ‘crust’ of larger particles dominates the outer layers, and the fraction of the surface with exposed ice decreases. One then expects that short-period comets, which have been resident the inner Solar System for multiple orbits, will have surface physical properties significantly different from Trans-Neptunian Objects (TNOs) or from dynamically new comets from the Oort cloud. The albedos of small TNOs (including Centaurs) are much higher than those of short-period comets (Brown et al. 2006), which supports the model of rapid surface evolution.

New insight into the nature of comets was provided by the discovery of cometary debris trails (Sykes et al. 1986). Unlike the small-particle tails apparent at visible wavelengths, debris trails consist of large (mm-cm), dark, low-velocity particles more readily observable at thermal infrared wavelengths. A survey of trails detected serendipitously by the *Infrared Astronomical Satellite* concluded that cometary mass loss was primarily in the form of these large particles and that comets therefore had a greater refractory or rocky component than previously thought, with a dust/gas mass ratio of $\sim 3/1$, consistent with a formation location similar to Pluto and Triton (Sykes and Walker 1992). One of the best-observed comets of all time, C/Hale-Bopp, yielded a wealth of new observational data, including submillimeter photometry suggesting large particles dominate the mass of the coma of C/Hale-Bopp, with dust/gas > 5 (Jewitt and Matthews 1999).

It was also recognized that these trails are the first stage in the evolution of a meteor stream. While dust trails were immediately recognized as the ‘genetic link’ between comets and meteor streams (Sykes et al. 1986), many meteor streams have been associated with comets since the mid-nineteenth century, when their radiants were measured and found to coincide with known comet orbits (Yeomans 1991). For more historical details, we refer the reader to an excellent review of this field by Jenniskens (2006). Kresak (1993) showed that debris trails would actually produce meteor *storms* (analogous to the well-known Leonids) if they intersected the Earth’s orbit: the width of debris trails matches the duration of meteor storms (less than an hour) but is less than that of showers (days), and the particle density within debris trails better matches the extremely high zenith hourly rate of meteor storms rather than the order-of-magnitude-lower meteor rate in meteor streams. Meteor storms also appear to be associated with relatively recent cometary events, and their orbits match the current orbits of associated comets. Meteor streams, on the other hand, significantly deviate in mean orbit from that of their associated comet, as well as having a wide dispersion. The Taurid meteor complex is widely associated with emissions from

comet 2P/Encke, not in its present orbit, but rather that of 10^{4-5} yr ago (Steel et al. 1991; Jones 1986).

Spacecraft with cameras and dust sensors have now encountered five comets: *Giotto* passed 600 km and *Vega* passed 8000 km from 1P/Halley in 1986 (McDonnell et al. 1987; Mazets et al. 1987); *Giotto* subsequently passed within 100-200 km of Grigg-Skjellerup in 1992 (McDonnell et al. 1993); *Deep Space 1* passed 2100 km from 19P/Borely in 2001 (Soderblom et al. 2002); *Stardust* passed 236 km from 81P/Wild 2 in 2004 (Brownlee et al. 2004); and then *Deep Impact* met 9P/Tempel 1 in 2005 (A’Hearn et al. 2005). The size distribution of detected particles indicates most of the mass of cometary dust is in the largest particles. Thus, nearly all estimates of cometary dust mass loss based on ground observations at visible wavelengths are lower limits to the actual dust mass loss. Particularly important, then, is the size of the largest particles. A particle of order 5 mg struck the front bumper of *Giotto* as it approached comet Halley; the particle perturbed the spacecraft attitude, generated an ion cloud detected by the spacecraft, and damaged the spacecraft’s star tracker (Goldstein et al. 1991). During the flyby of Grigg-Skjellerup, the Radio Science Experiment detected a particle of at least 30 mg (Patzold et al. 1993). During the recent *Stardust* encounter with 81P/Wild 2, there is evidence of a 14 mg particle on the dust shields (Anderson et al. 2004). The dust flux monitor yielded a large-particle-dominated size distribution with cumulative mass index 0.75; these results also led to the prediction that the dust collector may contain a mm-size particle, which will dominate the total collected mass (Green et al. 2004). As the Deep Impact impactor spacecraft approached 9P/Tempel 1, large particles caused dramatic attitude jogs (A’Hearn et al. 2005). Such particles would all be bright meteors if they were to enter the Earth’s atmosphere. Large enough to be only slightly affected by radiation pressure, they follow orbits similar to their parent nucleus and only gradually drift away. The estimated dust/gas mass loss ratio is > 3 from these impact observations, consistent with the value inferred from remote observations

of debris trails by *IRAS*, suggesting that comets are mostly composed of rocky material. Furthermore, the dust-to-gas mass ratio of ejected material underestimates that of the nucleus, since it does not include objects too large to be lifted off the nucleus (unless there are simply no particles larger than 1 g within the nucleus).

Debris trails provide a unique record of comet emission history in addition to providing insights into their composition. Over the eight trails detected by *IRAS* associated with known short-period comets, Sykes and Walker (1992) determined the ages of the oldest detected particles to be from years to centuries. They inferred that all short-period comets should have trails, and while the median dust to gas mass ratio for the comets studied was 3, individual values ranged from 1.2 to 4.6 - indicating perhaps a significant variation in composition from comet to comet. In this paper we report on the first survey of short-period comets since *IRAS* made its observations more than 20 years ago, focusing on the large particle emissions of these objects. Taking advantage of the greater sensitivity, spatial resolution and pointing capability of the new *Spitzer Space Telescope*, we have quadrupled the detections of short-period comets and have been able to probe the similarity of the large particle emissions of short-period comets in more detail than has been possible previously.

2. Observations

2.1. Methods of observation and data reduction

All observations presented here were performed with the Multiband Imaging Photometer for *Spitzer* (MIPS; Rieke et al. 2004) at 24 μm . The dates and viewing geometries are summarized in Table 1. The observed comets were selected to be all those short-period (Jupiter-Family) comets in the inner Solar System ($r < 3.5$ AU) visible to *Spitzer* during the time period from 2004 Jan to 2005 May, corresponding to the initial

guaranteed-time and first general-observation cycles on the observatory; 34 comets met these criteria.

All comets were observed using the small-field photometry mode of MIPS, wherein each $6' \times 6'$ field is observed using a set of 2 telescope positions with 7 scan-mirror dithers at each. The first set of observations (PID 210; up to 9/21/2004, excluding 141P), executed during guaranteed time, covered only 3 fields per comet, with offsets in telescope coordinates (roughly, ecliptic longitude) centered on the nucleus, leading and trailing the nucleus by one field of view. For the remaining observations executed during general observing time (PID 20039), maps were built using $6'$ tiles designed to follow each comet's orbit to at least 10^6 km following the nucleus and $10'$ leading the nucleus. Thus a wider field on the sky, following the nucleus, was observed for the nearby comets.

The basic calibrated data (individual 128×128 pixel calibrated array images) were improved as follows. We noted a significant gradient across the individual images; the gradient is strongest at the beginning of a scan-mirror-driven dither pattern and gradually decreases. To reduce the effect, we median-combined all images from our project at each of the 7 scan-mirror positions (and for each exposure time), and subtracted these bias corrections from each original image. This correction is imperfect due to the prevalence of bright cometary emission (even after excluding the brightest comets), but improved the image quality significantly. To ensure that the bias subtraction did not remove some of the trail brightness, we inspected each bias image to determine the amplitude of structure, on $< 1'$ scales, is < 0.05 MJy sr $^{-1}$. (A large-scale gradient is present, but it has no bearing on our results as we will subtract a large-scale gradient from the final mosaics.) The mosaics were composed of 14 independent combinations of bias-subtracted images, so the amplitude of bias-image structure that survives into the mosaics < 0.01 MJy sr $^{-1}$. Further, there was no evidence of 'trail' like structure (by which we mean the structures presented in the

images in this paper) in the bias images.

The basic calibrated data were then shifted to each comet’s rest frame by shifting each image to counter the motion of the comet between the time an image was taken and the first image of the sequence. The images were mosaiced using the SSC tool *mopex*, which matches the backgrounds in overlapping portions of images and combines the images into a single celestial grid with outlier rejection to remove cosmic rays and galactic protons (Makovoz and Khan 2005).

3. Dynamics of large particles

Particles of different size can be distinguished in the images due to the size-sensitive effects of radiation pressure. As a first-order approximation—which is relatively accurate for large particles far from the comet but becomes inaccurate for particles that are small, recently ejected, or close to the comet—we neglect the ejection velocity and assume the particles come into existence with the same orbit as the nucleus. They immediately experience radiation pressure from sunlight, with a r^{-2} dependence identical to solar gravity and force ratio

$$\beta \equiv \frac{F_{rad}}{F_{grav}} = \kappa \frac{Q_{pr}}{\rho s}, \quad (2)$$

where Q_{pr} is the effective efficiency of sunlight absorption and scattering for radial-directed momentum transfer (assumed to be unity for large particles), ρ is the particle density in g cm^{-3} , and s is the particle radius (in μm), and $\kappa = 0.57$ (Burns et al. 1979). Very large particles, with $\beta \rightarrow 0$, will follow nearly the same orbit as the nucleus, feeling negligible radiation pressure. (In detail, they will still deviate, because of the ejection velocity of the particle and non-gravitational forces due to asymmetric outgassing acting on the nucleus.) As discussed above, the largest particles that can be lifted from the nucleus due to sublimation are of order cm size, so $\beta > 5 \times 10^{-5}$ for $\rho \leq 1 \text{ g cm}^{-3}$. The orbits of

particles with such small β cannot be easily distinguished from the nucleus orbit without observations over long periods. As the particles separate from the nucleus, the effect of planetary perturbations increases and can ultimately result in dispersal of the trail. To first order, the largest particles in the trail lie along the orbit of the nucleus, and we consider the particles that have been dispersed due to perturbations as part of the more diffuse zodiacal cloud. Equivalently, in the terminology of meteor science, the largest particles lie within the same storm or shower, and the particles that have been dispersed due to perturbations are sporadic meteors. Nuclear fragments will follow approximately the same orbit, with modification due to the initial velocity of splitting, non-gravitational forces due to asymmetric outgassing, and planetary perturbations over time. In general the large debris from recent orbits will be splayed along the comet’s orbit.

To track the locations of particles with finite β , we predict their trajectories as follows. Over the two year period preceding observation, we calculate the detailed motion of 10^4 particles produced at even intervals (one particle every 2 hr), for each of $\beta = 10^0, 10^{-1}, 10^{-2}, 10^{-3}$, and 10^{-4} . We assume each test particle’s initial velocity and position is the same as the nucleus, including non-gravitational effects, if known. The x, y, z locations of all particles are then projected onto the sky for the geometry of the *Spitzer* observation. Particles of a given size generally lie along a simple arc on the sky. This arc of particles with common β is the *zero-velocity syndyne*. The syndynes were generated and overlaid on each comet image. They trace the locations and shapes of both the comet tails and trails. They do not match the inner cometary comae, which are due to recently-ejected, small particles with non-negligible ejection velocity and some memory of their origin on the rotating nucleus in asymmetrically located jets. Figure 1 illustrates the zero-velocity syndynes and their projection on the sky for one of our survey comets.

To supplement the zero-velocity syndynes, we also generated Monte-Carlo simulations

of particles produced over the 1-year period prior to observation. The computational techniques are described by Kelley et al. (2007). For the Monte-Carlo simulations, 10^6 particles were emitted over the 1-year period, with a power-law size distribution from $10^{-4} < \beta < 10^{-1}$ with mass index $\alpha = -1$, which distributes mass evenly among particle sizes but favors smaller particles for surface area. The velocity distribution is directed toward the Sun, falling off as the cosine of the zenith angle and with peak velocity $v_{ej} = 1.0\sqrt{\beta/r}$ km s $^{-1}$, where r is the distance from the Sun at the time of particle ejection. For typical trail particles produced at $r = 1$ AU and with $\beta = 10^{-4}$, the ejection velocity is 10 m s $^{-1}$. These Monte Carlo simulations are not adequate to trace the debris trails over their entire ages, but rather they provide a somewhat improved guide to the beginning of the trail, near the nucleus. Longer-term simulations can follow the evolution of the debris but are computationally expensive (e.g. Vaubaillon et al. 2005).

4. Measured debris trail properties

For each debris trail, we measured the brightness and width in one-dimensional slices perpendicular to the orbit (coadding along the orbit by 30-90 pixels [2.5"/pixel] depending on signal-to-noise). Table 2 shows the slice locations in apparent angular distance from the nucleus, ϕ , and physical distance $\phi\Delta$, along the orbit projected on the sky, where Δ is the distance to the observatory at the time of observation. For each profile, a Gaussian fit was made, and Table 2 lists the peak surface brightness I_ν (median 0.12 MJy sr $^{-1}$, range 0.02-0.9 MJy sr $^{-1}$) and full-width-at-half-maximum in angular units W (median 27", range 7-78") and physical units $W\delta$ (median 5×10^5 km, range 0.9-15 $\times 10^5$ km), in the viewing plane perpendicular to the line of sight. When fitting the Gaussians to the slices, a polynomial was simultaneously fitted to portions of the slice on either side of the trail. The optical depth, τ , was derived by assuming the grains are blackbody emitters with

temperature $T = 300r^{-1/2}$ K, as was measured for trails with multi-band IRAS detections (Sykes et al. 2005). Note this temperature is significantly warmer than that obtained by dust (grey, isothermal particles), for which the temperature at 1 AU $T_1 < 278$ K. As discussed by Sykes et al. (2005), trail particles are more consistent with rapidly rotating, randomly oriented, zero-albedo particles maintaining a latitudinal temperature variation across their surfaces. Table 2 lists the resulting τ (median 2×10^{-9} , range $0.3\text{-}16 \times 10^{-9}$). The 1-dimensional flux of the trail, $F_{1D} = I_\nu W$, measures the flux per unit length along the trail; Table 2 lists F_{1D} (median 4.6 mJy/arcmin, range 0.4-62 mJy/arcmin).

4.1. Debris age

First, we estimate the particle ages analytically, to determine how the trajectories of debris evolve as a function of the ratio of radiation pressure to gravity, β , the ejection velocity, v_{ej} , and the comet’s orbit’s perihelion distance and eccentricity, q and e . For particles ejected at perihelion, in the direction of the comet’s motion, with velocity v_{ej} , the rate of separation in mean anomaly of a particle from the nucleus is

$$\frac{d\theta}{dt} = \sqrt{\frac{GM}{a^3}} \frac{2+e}{1-e} \beta + 3 \frac{v_{ej}}{a} \left(\frac{1+e}{1-3} \right), \quad (3)$$

where the first term is due to radiation pressure and the second one is due to the ejection velocity (eq. 1 and 2 of Sykes and Walker 1992). If the ejection velocity scales as

$$v_{ej} = v_1 \beta^{1/2} q (AU)^{-1/2} \quad (4)$$

(cf. Whipple 1951) where for example Reach *et al.* (2000) used $v_1 = 1 \text{ km s}^{-1}$ for 2P/Encke, then

$$\frac{d\theta}{dt} = \sqrt{\frac{GM}{a^3}} \frac{2+e}{1-e} \beta \left[1 + 3v_1 \left(\frac{GM}{1 \text{ AU}} \right)^{-1/2} \beta^{-1/2} \frac{\sqrt{1+e}}{2+e} \right]. \quad (5)$$

For the comets in our sample, particles with $\beta = 10^{-3} \beta_3$ separate from the nucleus at a rate

$$\frac{d\theta}{dt} = 0.27 \left[1 + 1.6 \frac{v_1}{\text{km s}^{-1}} \beta_3^{-1/2} \right] \beta_3 \text{ deg yr}^{-1}, \quad (6)$$

where $\beta_3 \equiv \beta/10^{-3}$, indicating that the radiation pressure and ejection velocity terms are comparable. The median $d\theta/dt = 0.7'/\text{yr}$.

We can then approximately convert the change in mean anomaly to the separation, ϕ , on the sky using (geometrically)

$$\frac{d\phi}{d\theta} = \frac{r}{\Delta} \frac{df}{d\theta}, \quad (7)$$

and the derivative of true anomaly per unit mean anomaly

$$\frac{df}{d\theta} = \frac{1 + e \tan \frac{E}{2} \cos^2 \frac{f}{2} \frac{r}{a}}{1 - e \cos^2 \frac{E}{2} \tan \frac{f}{2} \frac{r}{a}}. \quad (8)$$

The median value for our observations is $d\phi/d\theta = 1.1$ (with a range 0.66 to 2.06). Combining these equations, the median $d\phi/dt = 0.8'/\text{yr}$.

We now estimate the ages of the oldest observed particles from numerical orbit integration, which should be more accurate, because fewer approximations are required. The orbits of particles with $\beta = 10^{-3}$ were integrated to the present beginning on an ejection date ranging from 1 day to 2 years into the past. For these calculations an ejection velocity of zero and a comet mass of zero are assumed, i.e. the particles simply separate from the nucleus according to gravity from the Sun and planets, and radiation pressure from the Sun. Their coordinates on the date of the *Spitzer* observation were then compared to those of the nucleus, yielding the separation (on the projected sky-plane) from the nucleus as a function of the particle age. This separation of any given particle increases with time, but particles produced at perihelion separate from the nucleus more quickly and overtake those produced just earlier. Figure 9 shows the separation versus age for 129P/Shoemaker-Levy 3. For comets observed pre-perihelion, such as 129P, the separation versus age is roughly linear for young particles. The separation is noticeably nonlinear for particles produced near perihelion, which makes the trail expansion rate especially nonlinear for comets observed post-perihelion. With the notable exception of 2P/Encke, the rate of separation is monotonic over the region covered by the *Spitzer* images, allowing an accurate

numerical derivative. For all comets, we estimate $d\phi/dt$ using the geometric mean of the separation/age for particles that are $1'$ and $10'$ from the nucleus. The resulting values have median $d\phi/dt = 15'/\text{yr}$, with a range $5.7\text{--}40'/\text{yr}$. The numerical results need to be increased to take into account the effect of nonzero ejection velocity. Based on the equations above, the increase in separation for $v_1 = 1 \text{ km s}^{-1}$, $\beta = 10^{-3}$, and sunward-hemisphere ejection, is a factor of 2.6.

The numerical determinations of the rate of separation are consistently higher than the analytic estimate. Further, the numerical determinations of the separation rate for $\beta = 10^{-3}$ and $\beta = 10^{-4}$ do not scale with β as the analytic relations predict (being instead much more shallow). In order to reach the analytic estimate, some approximations were made, which apparently led to the difference. We will use the numerical results from the orbit integrations in this paper. The trail profiles in Table 2 cover $\phi \sim 10'$ from the nuclei. Thus the observed debris trail particles are $\sim 0.6(10^{-3}/\beta)$ yr old. Taking into account the sizes of the *Spitzer* images for the various comets, the range of ages is 0.3–2 yr. This does not mean that all (or even most) of the particles were emitted 0.6 yr ago, but only that a particle with $\beta \sim 10^{-3}$ emitted 0.6 yr ago would be at the observed location; particles a factor of 2 smaller or larger in size than $\beta = 10^{-3}$ (or ejected with velocities smaller or larger) would be correspondingly further behind or closer to the nucleus.

In many cases, the debris trails continue to the edges of the *Spitzer* image, so older particles are certainly present, as clearly demonstrated by the *IRAS* trails that extend from more than 1° up to 90° of the comet orbit in mean anomaly, corresponding to minimum trail ages of 2.6–140 yr (Sykes and Walker 1992). The trail ages exceed the orbital period for many comets, so a given trail contains debris from many revolutions.

Further evidence of the longevity of debris trail particles is that trails are present even for comets observed far before perihelion. Figure 10 shows that there is no significant

asymmetry in the trail optical depth with respect to perihelion. While comets show a wide range of behaviors pre- and post-perihelion, none of them are active *only* at aphelion. Thus, the material observed in a trail on the present revolution was largely produced on previous revolutions. This is in contrast to the dust tails and comae, which are ephemeral and only due to the present revolution. The near-nuclear observations we present here contain $\beta = 10^{-3}$ particles from the present and previous revolution, for comets observed post-perihelion, and particles from the previous revolution, for comets observed pre-perihelion. They also contain $\beta \leq 10^{-4}$ particles from previous revolutions.

An upper limit on the debris trail age is set by gravitational perturbations. If debris trails were due only to very large particles, e.g. with $\beta < 10^{-5}$, then trails arise from many revolutions of the comet. In this case, the trail particles would diffuse from the present comets' orbits due to differential gravitational perturbations. Indeed even minor perturbations and orbital shifts due to non gravitational and Yarkovsky forces (which will be different for meteoroids and the nucleus) make it very unlikely to have more than a few revolutions contributing to the debris trails, which follow the *current* orbit of the nucleus very closely. Instead, the trail would be distorted by minor perturbations and truncated by significant perturbations. Table 1 shows the date, T_{pert} , of the last passage of each comet within Jupiter's Laplacian gravitational sphere of influence (0.32 AU) as calculated by K. Kinoshita¹. We see that the date of the last significant perturbation by Jupiter was before 1950 for all but 7 comets. (62P, 65P, 67P, 103P, 111P, 116P, and 120P), and these comets present a range of trail properties similar to the rest of the sample, including one comet with a very bright leading+following trail (65P) and one nondetection (103P). Minor perturbations, within 1 AU of Jupiter, are much more common; the median time since such a perturbation for our sample comets is 35 yr.

¹<http://www9.ocn.ne.jp/comet/index.html>

Sykes and Walker (1992) set an independent upper limit on the trail ages, and a lower limit on β , by requiring particles ejected at perihelion have enough time to reach both the furthest leading and following extents of the observed trails. They found ages of 11–660 yr with a median of 74 yr. These ages are often greater than the time since the last minor perturbation (within 1 AU of Jupiter), suggesting such minor perturbations are not effective at dispersing trails.

4.2. Debris mass production rate

The masses of the debris trails are estimated as follows. A straightforward estimate of the mass per unit projected angle on the sky, ϕ , assuming a tapered cylindrical shape for the trail, yields

$$\frac{dM}{d\phi} = \frac{\pi}{3}\kappa W \Delta^2 \tau \beta^{-1} = 1.1 \times 10^9 W(\text{arcsec}) \Delta(\text{AU})^2 \left(\frac{\tau}{10^{-9}}\right) \left(\frac{10^{-3}}{\beta}\right) \text{ g/deg.} \quad (9)$$

Since the brightness profiles are only taken in the debris trail, only the values of $\beta = 10^{-(3-4)}$ that are consistent with the centroid, width, and length of the trail apply.

We list the mass per unit apparent separation in Table 2 as $dM_3/d\phi$, for an assumed particles size $\beta = 10^{-3}$. For many of the images, this is an upper limit to β , and therefore $dM_3/d\phi$ is a lower limit to the mass. The values of $dM_3/d\phi$ are independent of the particle dynamics. For all the trail profiles in Table 2, the median value $dM_3/d\phi = 21 \times 10^{10}$ g/deg, and the range is 0.6–430 $\times 10^{10}$ g/deg.

We can now use the particle separation rates (from the numerical integrations discussed in the previous section), $d\phi/dt$, together with the observed mass per unit separation, $dM_3/d\phi$, to estimate the mass-loss rates, dM/dt , required to produce the debris trails. The median $dM/dt = 4 \text{ kg s}^{-1}$, and the range for all the comet profiles is 0.2–36 kg s^{-1} . Note that $dM/d\phi \propto \beta^{-1}$ while the analytic estimate $d\phi/dt \propto \beta$, so the mass loss rate dM/dt

should be independent of the assumed particle size. However the numerical estimates of $d\phi/dt$ show much less dependence on β , with the data in Figure 9 yielding $d\phi/dt \propto \beta^{0.3}$ and suggesting the mass-loss rates scale as $(\beta/10^{-3})^{-0.7}$.

For comparison, using his "inverse tail method" to compare dynamical models to surface brightness images, Fulle (1996) measured as meteoroid mass production rate of 100 kg s^{-1} near perihelion for 10P/Tempel 2, and Fulle (1990) measured meteoroid mass production rates of $30\text{--}50 \text{ kg s}^{-1}$ for 2P/Encke and 6P/D'Arrest; those results are in general agreement with ours, being somewhat higher because they refer to dust production closer to perihelion. Sykes and Walker (1992), using the *IRAS* observations of entire debris trails for 8 comets, measured meteoroid mass production rates of $4\text{--}250 \text{ kg s}^{-1}$. For the 5 comets in common between the *IRAS* and *Spitzer* surveys (2P, 9P, 10P, 65P, and 67P), the dM/dt inferred in this paper are comparable (this paper/SW92 = 0.1, 1.8, 2.3, 0.6, 8, respectively). The comet for which the mass-loss rates are most discrepant is 2P/Encke. Reach *et al.* (2000) used ISOCAM observations and Monte Carlo simulations of 2P/Encke to obtain $200\text{--}600 \text{ kg s}^{-1}$ for the 1997 apparition, in agreement with Sykes and Walker (1992)'s value of 260 kg s^{-1} . The low value for 2P/Encke in the present paper is likely due to observing only a small portion of the trail, hence sampling a very restricted range of emission history. The high value for 67P is likely due to a line-of-sight enhancement or 'neck-line' as discussed below. The overall agreement between the different observations and calculations in this paper and Sykes and Walker (1992) is encouraging.

Total trail masses are discussed for individual comets in §5. Since our *Spitzer* images generally cover only limited portions of the orbits, and many trails clearly extend to the edges of the images, we can estimate in general only lower limits to the trail mass. (This effect goes in the same direction [underestimating the mass] as our conservative assumption of $\beta = 10^{-3}$.) For the 6 comets with reasonable total mass estimates, the range is 4×10^{10}

g to 9×10^{13} g. Lower limits for the others range from $> 2 \times 10^{10}$ g to $> 8 \times 10^{11}$ g. The trail lengths found in the *IRAS* survey were of order degrees (in mean anomaly), so the total trail masses from the present survey are of order $dM/d\theta$ (with θ in degrees), i.e. typically 10^{11-12} g. These masses extend to about 1 order of magnitude lower than those of the *IRAS*-detected trails (Sykes and Walker 1992), due to the greater sensitivity of the present survey. The masses remain lower limits, because even larger (cm-sized) particles may be present, and there could be a fainter component of the debris trails extending over a large fraction of the orbit, which our observations do not cover. The existence of meteor showers over large fractions of comets’ orbits testifies to the existence of such an extended population of debris.

4.3. Comparing meteoroids to ice

The mass-loss rate in large particles can be compared to that due to ice sublimation as follows. If the H_2O production rate is $Q_{\text{H}_2\text{O}}$, then the mass loss rate of sublimating ice is

$$\frac{dM_{ice}}{dt} = 2.9 \times 10^2 \frac{\langle Q_{\text{H}_2\text{O}} \rangle}{10^{28}} \text{molecule s}^{-1} \text{kg s}^{-1}, \quad (10)$$

where $\langle Q_{\text{H}_2\text{O}} \rangle$ is the mass production rate averaged over the orbit. For the Jupiter-family comets studied by A’Hearn et al. (1995), the peak H_2O production rate (obtained by extrapolating observed production rates to perihelion using the estimated dependence of Q on r) has a median of $Q_{\text{H}_2\text{O}}(\text{peak}) \sim 0.5 \times 10^{28}$ and a range from $(0.02-5) \times 10^{28}$ molecule s^{-1} . To estimate the average H_2O production rate over the orbit, we assume the production rate scales as $Q \propto r^{-\alpha}$, with α taken from Table V of A’Hearn et al. (1995) or set to the nominal value of 2.7; we also set the ice production to zero when $r > 3$ AU. Table 3 shows the results for comets studied both by A’Hearn et al. (1995) and the present work. The values of α are highly uncertain, because comets generally exhibit temporal variations that are very different from power-laws. Further, the values of $Q_{\text{H}_2\text{O}}$ are rather

uncertain and may be statistically biased toward higher values by selection effects. The median $dM_{ice}/dt = 9.1 \text{ kg s}^{-1}$ with a range from 1.2–390 kg s^{-1} .

For comparison, Kresák and Kresáková (1987) calculated dM/dt by averaging over orbits in a similar manner. Instead of using the ice production rate $Q_{\text{H}_2\text{O}}$, they use a rough calibration of cometary total visual magnitudes, using 1P/Halley as a calibration source and assuming a production rate $\propto r^{-4}$. Each revolution is calculated with its appropriate osculating orbital elements, over the 100 yr period from 1885–1985. The visible magnitudes are a measure of the total scattering by dust, and Kresák and Kresáková (1987) convert them to mass loss rates assuming a gas-to-dust mass ratio of 3:1. Their ice mass loss rates are included for the relevant comets in Table 3. The mass-loss rates inferred from the visual magnitudes and the H_2O production rates do not agree very well. Only a small part of the difference is due to assumptions about α ; we found less than a factor of 2 variation in dM/dt for a wide range of α , with the median changing from 9.1 to 7.2 kg s^{-1} if we set $\alpha = 4$ for all comets.

Given the wide range of dM_{ice}/dt estimates, debris-to-ice ratios for individual comets cannot be considered accurate. But there are enough comets in the sample that outliers can be identified and a statistical result can be obtained. Taking the ratio of the median dM/dt and dM_{ice}/dt , the debris-to-ice mass ratio is 0.5. But this ratio of medians may not be particularly meaningful, due to the wide range of actual mass-loss rates for comets and the discrepancies between methods for estimating the ice mass loss rates. There may be a wide diversity of meteoroid:ice fractions among comets, and detailed studies of individual comets are needed to make reliable measurements. The infrared survey results presented in this paper demonstrate that meteoroids are at least comparable to ice mass production in a large sample of Jupiter-family comets.

4.4. Trails and ‘neck-lines’

Brightness enhancements near a comet’s projected orbit plane are not necessarily old debris trails. The particles’ orbits are only slightly different from that of the nucleus: the radiation pressure and the in-orbit-plane components of the ejection velocity will tend to spread particles only within the orbit plane, and only the out-of-plane component of the ejection velocity (and gravitational perturbations by the planets) will cause perpendicular spread. Particles released with a non-zero velocity perpendicular to the comet orbit will still cross the orbital plane every 180° of true anomaly. If the nucleus is observed at a true anomaly of f_0 then particles emitted at true anomaly $f_0 - 180^\circ$ will form a thin ridge of high column density when viewed at a low orbital plane angle. The thin ridge has been named a ‘neck-line structure’ (Kimura and Liu 1975; Pansecchi et al. 1987; Fulle 1987). A neck-line requires particles produced at true anomaly $f_0 - 180^\circ$, and a low angle of the line of sight with respect to the orbit plane.

The infrared emission in some of our comet images occupies narrow, linear structures that are not precisely aligned with the projected orbital plane at the time of observation. These were prime candidates for neck-line structures. In each case, a Monte Carlo simulation was performed and the particles produced near a true anomaly 180° from the nucleus (at the time of observation) were isolated. Separate sky-plane images were made for the neck-line particles and the remainder (debris trail particles). The debris trails follow the orbit of the comet precisely, but the neck-lines are often at a nonzero position angle with respect to the orbit. Experiment showed that the neck-line position angle was usually very close to that of the $\beta = 10^{-3}$ syndyne. For 67P, Kelley et al. (2007) have cleanly separated neck-line and debris trail using infrared images, while the optical image was dominated by the neck-line. For comets whose infrared emission follows the nucleus but is closer to the $\beta = 10^{-3}$ syndyne than the trail, we found the simulations are consistent with a neck-line

structure rather than strictly a debris trail. There will inevitably be a mixture of both the nodally enhanced neck-line and the debris trail, from particles produced over the remainder of the orbit not close to $f_0 - 180^\circ$. A neck-line structure is essentially a portion of the debris trail with brightness enhanced due to projection effects. The neck-lines observed in our survey have ages that range from 1.1 to 3.3 yr, and are observed within a few arcmin of the nucleus. Therefore, these structures are necessarily comprised of large ($\beta < 10^{-3}$) particles.

Both neck-lines and debris trails require large particles, and the mass estimates per unit path length $dM/d\phi$ and total mass taking into account the extent on the sky are calculated in precisely the same manner as in the previous section. The neck-lines we observe are old (> 400 days, but < 1 orbit) and are composed of large particles that trail the comet, with distinct orbits reflective of their ejection at a selected time when their orbit planes were along the line of sight. In theory, neck-lines are composed of particles emitted from a single instant, and a plot of the neck-line intensity versus distance from the nucleus is essentially a plot of intensity versus β . But in practice the ejection velocities and subsequent trajectories must be modeled relatively accurately to allow such an inversion to the particle size distribution. Such work is beyond the scope of this paper. (Note also that the mass-loss rate, dM/dt , from the previous section does not strictly apply to neck-lines.) The presence of neck-lines for individual comets is discussed below.

5. Descriptions of individual comets

2P/Encke (Fig. 2) shows a debris trail that spans the image, as well as a highly-elongated pseudo-coma. The *Spitzer* MIPS and IRAC images are discussed in detail in Reach *et al.* (2007); earlier results from *ISO* are discussed in Reach *et al.* (2000); and the first detection from *IRAS* is discussed in Sykes and Walker (1992). The brightness and inferred mass per unit mean anomaly are relatively flat across the image. The *Spitzer* image

measures only a small fraction of the total mass of the trail, which was seen to extend over 93° of mean anomaly in the *IRAS* data. The total trail mass, estimated using the *IRAS*-observed mean anomaly range and 1/2 the *Spitzer*-observed $dM_3/d\theta$ (to account for a falloff of trail brightness with distance behind the nucleus), is 7×10^{13} g.

4P/Faye (Fig. 8) shows a distinct debris trail leading the nucleus. Following the nucleus, there are both a bright tail *and* a distinct trail, as can be seen from the projected syndynes. The trail of this comet was the first to be detected optically, extending over 10° with $2'$ width in 1991 Spacewatch images (Rabinowitz and Scotti 1991). Figure 8 shows the trail both leading the and following comet, as was seen for 2P and 10P, both of which had long trails in the *IRAS* data, supporting a common origin for the Spacewatch and *Spitzer* trails.

9P/Tempel 1 (Fig. 2) shows a faint debris trail due to its relatively large heliocentric distance ($r = 3.75$ AU). It was included in the survey despite being somewhat outside our $r < 3.5$ AU selection criteria, as part of preparation for the *Deep Impact* mission (A'Hearn et al. 2005). The debris trail was known from *IRAS* in 1997, and the optical depth inferred from our data is consistent with that inferred from *IRAS* (Sykes and Walker 1992). Multiple-epoch observations with *Spitzer* are under way to monitor the evolution of the debris trail. The trail extends beyond the edge of the image; using the *IRAS*-observed length in mean anomaly (7°) the total mass is 1×10^{13} g.

10P/Tempel 2 (Fig. 2) shows a long debris trail similar to 2P/Encke, spanning the image and with significant brightness leading the nucleus. This trail was seen by *IRAS* in 1983, with comparable optical depth, spanning 60° mean anomaly (Sykes 1990) making it the longest and best-detected of the *IRAS* debris trails (Sykes and Walker 1992). Less material is leading the nucleus than following it, and the mass profile increases somewhat toward the ‘following’ edge of the image. To calculate the mass of debris leading the

nucleus, we use a constant $dM_3/d\theta = 8 \times 10^{11}$ g/deg (from the *Spitzer* image) and a length of $5.4\circ$ mean anomaly (from the *IRAS* data). To calculate the mass of debris following the nucleus, we use a constant $dM_3/d\theta = 1.5 \times 10^{12}$ (from the *Spitzer* image) and a length of $60\circ$ mean anomaly (from the *IRAS* data). The total mass is 9×10^{13} g.

32P/Comas Sola (Fig. 2) presented a very large and bright coma and tail from small particles. The coma is fan-shaped, with the opening angle not in the anti-solar direction but rather approximately perpendicular to the projected orbit. The *dust tail* is roughly bisected by the $\beta = 10^{-2}$ syndyne and bounded by the $\beta = 10^{-3}$ and $10^{-1.5}$ syndynes. The *debris trail* can be barely discerned but appears as a thin linear feature, closely following the comet’s projected orbit, with a gap in azimuth between the trail and tail and in radial distance between the trail and coma. This phenomenon is also seen in 2P/Encke (Reach *et al.* 2007) and is due to the large particles from the *present* orbit still being close to the nucleus, while the large particles from the *previous* orbits are already located along the comet’s orbit. The total extent of the debris trail is unknown, so we estimate only the lower limit of its mass using constant $dM_3/d\theta = 3 \times 10^{10}$ g/deg over a nominal 1 deg of mean anomaly.

36P/Whipple (Fig. 2) had a small round coma centered on the nucleus and a $5'$ long linear feature, $15''$ wide, extending behind the nucleus. The linear feature does not precisely follow the comet’s projected orbit, as expected for very large particles. Instead, it follows the zero-velocity syndyne for $\beta \simeq 10^{-2.7}$, which corresponds to particle size ~ 0.3 mm (assuming density ~ 1 g cm $^{-3}$), which we will refer to as ‘intermediate-sized’ particles; such particles are still within the range of radar meteor studies and are apparently common in cometary orbits (Brown *et al.* 2002). The position angle of the infrared feature matches that of a ‘neck-line’ structure due to particles produced 3.3 yr prior to observation. The mass profile following the nucleus is fairly flat, and the total extent of the emission is unknown,

so we estimate a lower limit to the mass assuming a nominal 1° length in mean anomaly and correcting to the slightly smaller particle size $M > dM_3/d\theta \times 10^{2.7-3} = 3 \times 10^{11}$ g.

42P/Neujmin 3 (Fig. 3) had a faint tail, $30''$ wide, extension following the nucleus. This is apparently a dust tail, as it does not follow the projected orbit. Enough area was covered, and the anti-solar direction was nearly opposite the projected orbit direction, so that an upper limit $I_\nu < 0.02$ MJy sr $^{-1}$ could be placed on the debris trail using the portion of the image away from the coma and tail.

48P/Johnson (Fig. 3) was bright and had one of the best viewing geometries, and cleanest separation between trail and tail, in the survey. The fan-shaped dust coma is roughly bounded by the $\beta = 10^{-1}$ to 10^{-3} syndynes. The debris trail is clearly distinct from the coma and follows the projected orbit very precisely, so it can only be composed of large particles with $\beta < 10^{-4}$. The trail is $17''$ wide; such narrow trails, frequently found in this survey, would have been highly beam diluted to *IRAS* so are not surprisingly not detected. The trail is fainter, but present, leading the comet, requiring non-zero ejection velocity. The trail extends to at least the edge of the image; an estimated lower limit to its mass, assuming constant mass per unit mean anomaly and a length of 1° mean anomaly, is 2×10^{11} g.

49P/Arend-Rigaux (Fig. 3) has a bright point-like nucleus with diffraction rings and a dust tail due to small particles, $\beta = 10^{-1}$ to 10^{-2} . There is no debris trail, despite excellent viewing geometry and high-quality data. We place an upper limit on the surface brightness, $I_\nu < 0.03$ MJy sr $^{-1}$ corresponding to an optical depth $\tau < 2 \times 10^{-10}$, which is lower than that of detected trails. Because the comet was close, the trail is expected to be wider than those for most other comets ($\sim 1'$, scaling other comets trail widths by Δ), but a very wide area ($30'$) was mapped and should have included the debris trail. The upper limit on the debris trail is therefore very strict, and an explanation for the lack of trail

is required. As discussed below, comets with more non-asteroidal orbits (lower Tisserand parameter), like 49P, seem to have weaker trails. It is quite possible that the close approach to Jupiter in 1997 is the root cause for the lack of a detectable trail. Particles from the previous revolution are normally the ones that would be detected in the debris trail on this revolution. The 1997 close approach may have perturbed the orbits of large particles from the previous revolution, scattering them to a different location or dispersing them widely.

53P/van Biesbroeck (Fig. 3) had a poor viewing geometry, with the tail and trail superposed to within 3° position angle. There was no debris leading the comet, down to an upper limit of 0.05 MJy sr^{-1} surface brightness, which corresponds to $\tau < 9 \times 10^{-10}$.

56P/Slaughter-Burnham (Fig. 4) has one of the most clear-cut debris trails, with an excellent viewing geometry. The debris trail is narrow, extends both leading and following the nucleus, precisely following the projected orbit as expected for particles with $\beta \ll 10^{-3}$ experiencing negligible radiation pressure. The lower limit to the trail mass, for $\beta = 10^{-3}$ particles and a length of 1° mean anomaly is $8 \times 10^{10} \text{ g}$.

62P/Tsuchinshan 1 (Fig. 4) was observed to have both a tail, roughly bounded by the $\beta = 10^{-3}$ to 10^{-1} zero-velocity syndynes, and a debris trail. The trail is separated from the tail following the comet, thanks to a favorable viewing geometry. It is however faint, and the trail mass can only be crudely bounded, if we assume $> 1^\circ$ mean anomaly length, as $M > 5 \times 10^{10} \text{ g}$.

65P/Gunn (Fig. 4) was observed with a very bright tail following the comet as well as a prominent debris trail leading the comet. The dust tail is slightly shifted from the orbit, mostly consistent with the zero-velocity syndynes of $\beta = 10^{-2}$ to 10^{-3} , but including the projected orbit ($\beta = 0$). The debris trail leading the comet is closely aligned with the orbit. This trail had been previously detected by *IRAS* (Sykes and Walker 1992). The trail extends to the edge of the *Spitzer* image without decreasing significantly in brightness.

Using the *IRAS*-observed lengths of 0.3° mean anomaly leading and 5.9° following the nucleus, together with the *Spitzer*-observed brightnesses, yields a total mass 9×10^{12} g.

67P/Churyumov-Gerasimenko (Fig. 4) had previously been found to have a debris trail by *IRAS* (Sykes and Walker 1992). The *Spitzer* observation is discussed in detail in a separate paper (Kelley et al. 2007). The portion of the debris trail leading the comet is evident, while the portion following the comet is contaminated by a neck-line structure and is therefore not solely a debris trail. The mass of the trail can be roughly estimated using its brightness leading the nucleus and the *IRAS*-observed length, yielding 1×10^{12} g.

69P/Taylor (Fig. 5) has a bright tail with a range of particle sizes, with the bulk falling within the $\beta = 10^{-2}$ to 10^{-3} zero-velocity syndynes. A debris trail precisely aligned with the orbit is clearly evident leading the comet; it is confused with the tail following the comet. Kresák (1993) discussed the case of *69P/Taylor*, which was observed split in 1916 but was subsequently perturbed by Jupiter in 1925 so that debris from the splitting should be widely dispersed. He mentions that a trail should be present but below the detection limit of *IRAS*. Our new observations are more sensitive, allowing us to detect the debris trail with *Spitzer*. If the comet were only discovered a few years ago, we would never know it had split in the past; this is an example of cometary calving, which is apparently frequent (Chen and Jewitt 1994). The total extent of the trail is not known, so we only estimate a rough lower limit for 1° mean anomaly of $M > 2 \times 10^{10}$ g.

71P/Clark (Fig. 5) was detected as a long debris trail, but without a bright nucleus or coma at the predicted location (using the orbit from 1998). Using the updated orbit after recovery in 2005 (?), a compact source at the nucleus' position is indeed present $2'$ ahead of that predicted from the 1998 orbit; this source is moving at the predicted rate based on the 2006 ephemeris. The most fascinating result for this comet is that its debris trail is long and even increases in brightness following the comet, peaking $11'$ behind it. This cannot be

explained by a simple dust production history. The 10^6 particle Monte Carlo simulation (with r^{-2} dust production) for this comet shows only a coma and trail, so the enhancement in trail behind the comet is not due to a geometric projection effect. The mass per unit mean anomaly seems to increase with distance following the nucleus, and the trail extent is unknown. A lower-limit mass for 1° mean anomaly is 8×10^{11} g. In 2006, this comet was observed again at much closer distance; Figure 8 shows a clearly-detected trail leading the nucleus. The trail following the nucleus cannot be cleanly discerned from a possible tail until near the edge of the image, at which point we see that the narrow ridge of emission extending across the entire image is indeed the debris trail, following closely the projected orbit of the comet.

78P/Gehrels 2 (Fig. 4) was exceptionally bright when observed, with a bright tail due to particles of indeterminate size (due to the unfavorable viewing geometry with the anti solar direction nearly parallel to the orbit-following direction). Leading the comet, there is a narrow feature that lies precisely along the projected orbit, which we identify as the debris trail. Using the mass per unit mean anomaly leading the comet, and a lower-limit length of 1° mean anomaly, yields a mass $M > 8 \times 10^{10}$ g.

88P/Howell (Fig. 5) was observed when it was relatively closeby, with unfavorable geometry (tail and trail overlapping), and covering a relatively small field of view. The extremely bright tail is likely due to small particles. The only portion of the image free of small particles is leading the comet, where there is a faint linear feature parallel to but slightly shifted (by less than its width) from the projected orbit of the comet. Based on comparison to images of other comets (*78P*, *123P*) viewed similarly and with clear ‘leading’ debris trails despite bright tails, we tentatively identify this feature as Howell’s debris trail. The lower-limit mass, derived as for *78P*, is $M > 8 \times 10^{10}$ g.

94P/Russell 4 (Fig. 5) has a moderately bright debris trail following the nucleus,

with no detectable emission leading the nucleus. The *Spitzer* observation was adversely affected by an observation of Saturn immediately preceding, but the image was adequately recovered. The trail is close to the projected orbit but follows the $\beta = 10^{-3}$ syndyne better. Based on comparison to simulations, much of the infrared feature is likely to be a neck-line structure due to particles produced 2.0 yr prior to observation. The estimated mass of the structure $> 3 \times 10^{10}$ g.

103P/Hartley 2 (Fig. 6) had a bright tail, roughly bounded by the zero-velocity syndynes for $\beta = 10^{-3}$ and 10^{-1} . The separation between the tail and trail was large enough to set an upper limit to the trail brightness relatively far behind the comet; no trail was seen leading the comet with an upper limit $I_\nu < 0.1$ MJy sr $^{-1}$.

104P/Kowal 2 (Fig. 6) had extensive infrared emission following the nucleus, but the apparent trail does not precisely follow the comet’s orbit. Instead, it is closer to the $\beta = 10^{-3}$ syndyne and may contain significant contribution from intermediate-sized particles. The mass estimate $M > 2 \times 10^{11}$ g is a lower limit because of the unknown total extent, though the surface brightness does decrease significantly before the edge of the image (suggesting most of the mass was observed). The orientation of the infrared feature is similar to that expected for a ‘neck-line’ from particles ejected 1.1 yr prior to observation, but the feature is broader than a neck-line. The feature is more likely a tail, due primarily to intermediate-sized particles.

(4015) *107P/Wilson-Harrington* was not strictly part of the short-period comet survey but was observed in the same manner. It was found to be a point source, with no extended emission along the orbit to a limit of $I_\nu < 0.05$ MJy sr $^{-1}$. At the observed heliocentric distance $r = 2.25$ AU, this corresponds to an optical depth limit $\tau < 4 \times 10^{-10}$.

108P/Ciffreo (Fig. 8) shows a narrow trail in the orbit of the comet. The bright source at the predicted location of the nucleus looks point-like and may actually be a celestial

source coincidentally close to the ephemeris position. A smaller, somewhat resolved source is located following the predicted location of the nucleus and within the debris trail. This object appears to be the actual nucleus, at least in terms of debris trail production, based on the location of some debris leading and most following its location. While the syndynes in Fig. 8 are centered on the predicted location of the nucleus, the flux reported in Table 1 is that of the smaller source. More detailed modeling is required to address these issues.

111P/Helin-Roman-Crockett (Fig. 6) has a thin trail extending to the edge of the image and precisely following the comet’s orbit. The brightness does not decrease significantly at the edge of the image, suggesting the trail may be massive; its narrow width shows it is also devoid of small particles. An estimate lower-limit to the mass $M > 3 \times 10^{11}$ g.

116P/Wild 4 (Fig. 6) was observed when relatively closeby and presented a very bright dust tail that makes it impossible to separately locate a possible debris trail.

120P/Mueller 1 (Fig. 6) has a prominent debris trail both leading and following the nucleus, closely following the orbit. Assuming a length at least 0.3° leading and 1° following the nucleus, the trail mass $M > 2 \times 10^{11}$ g.

121P/Shoemaker-Holt 2 (Fig. 6) had a bright elongated coma/tail due to particles of indeterminate size. While the anti solar and comet-following angles were not widely separated, a long enough field was observed to allow a debris trail in the comet’s orbit to be distinguished from a small-particle-only tail far from the nucleus. There is no clear, contiguous debris trail in the comet’s orbit, as there was for most of the other comets in the sample. However, there were two patches of emission along the comet’s orbit. The first patch is circular, located $9.8'$ following the nucleus, and the second one is elongated along the orbit, approximately $15.8'$ following the nucleus; their brightness ~ 0.2 MJy sr $^{-1}$ corresponds to an optical depth $\sim 2 \times 10^{-9}$. While these patches are aligned along the orbit, it is very likely (and cannot be determined with the present data) that

these patches are small interstellar clouds. Inspecting the *IRAS* images as reprocessed by Miville-Deschênes and Lagache (2005), there is significant, structured interstellar emission in the field.

123P/West-Hartley (Fig. 7) was observed relatively close by and had a very bright tail of small particles. The debris trail following the comet can be barely distinguished from the tail. Leading the comet, the debris trail precisely along the projected orbit, is detected without confusion from smaller particles. The presence of a significant trail leading the comet suggests the debris trail may be massive, but from the present observations only a rough lower limit can be made, by assuming a length 0.3° leading and 1° following the nucleus; this yields $M > 5 \times 10^{10}$ g.

127P/Holt-Olmstead (Fig. 7) was observed under very favorable geometric conditions, with the small-particle production being minimal at $r = 2.74$ AU and the anti solar (tail) direction 169° from the trailing direction. The brightness decreases significantly before the edge of the image, suggesting we have observed the bulk of the debris (though there could always be a fainter trail of larger particles). These factors combine to allow an actual measurement (rather than a limit) of the mass of $M \simeq 4 \times 10^{10}$ g. The extended emission stretches approximately along the orbit, completely inconsistent with a small-particle tail. But the orientation is not precisely along the orbit, being closer to the $\beta = 10^{-3}$ syndyne. The orientation of the infrared emission matches very well that of a ‘neck-line structure’ due to particles ejected 1.7 yr prior to observation.

129P/Shoemaker-Levy 3 (Fig. 7) had one of the best-defined debris trails owing to its brightness and favorable viewing geometry. The trail extends to the edge of the image without decreasing significantly in brightness, so only a lower limit to the mass can be made, assuming trail length at least 0.3° leading and 1° following the nucleus in mean anomaly, yielding $M > 5 \times 10^{11}$ g.

131P/Mueller 2 (Fig. 7) had very faint extended emission, evident only after smoothing the image. This faint emission is only present following the comet and would correspond to a lower limit to the trail mass assuming 1° length in mean anomaly of $M > 2 \times 10^{10}$ g.

133P/Elst-Pizarro has a very faint (~ 0.02 MJy sr $^{-1}$), narrow debris trail confined very precisely to the comet’s orbit. This comet has an orbit similar to main belt asteroids and exemplifies the class as defined by Hsieh and Jewitt (2006). The debris trail appears similar to other narrow trails in our sample, suggesting that the main belt comet lose significant mass in the form of large meteoroids, just like the Jupiter-family comets. More detailed modeling and image analysis are under way to better constrain mass production history.

P/2003 S2 (Fig. 7) had a debris trail precisely following the comet’s orbit. The brightness decreases significantly by the edge of the image, allowing a mass estimate $M \simeq 4 \times 10^{10}$ g, although faint trail emission extends to the edge of the image (so the total trail mass could be significantly higher). Part of the infrared emission may be due to a neck-line structure; it is not possible to separate them due to the viewing geometry placing the trail and neck-line on top of one another.

6. Statistical Trends of debris trail properties

We summarize properties of each comet that might influence the properties of their debris trails in Table 1. The orbital size and eccentricity are listed, together with the Tisserand invariant for gravitational scattering by Jupiter, T_J (Levison and Duncan 1997). And the date of the last passage of a comet into Jupiter’s gravitational sphere of influence is T_{pert} .

The amount of material in a given comet’s debris trail may be correlated with the present shape of the comet’s orbit. Figure 11 shows the debris mass production rate versus

q . Weak correlations are present between \dot{M} and a or q . The correlation coefficients between \dot{M} and a or q are -0.64 and -0.32, respectively; while the correlation coefficients between $\log \dot{M}$ and a or q are -0.66 and -0.62, respectively. This apparent correlation is unlikely to be purely a selection effect. While comets observed at large r could only be detected if they have relatively larger \dot{M} (at fixed sensitivity limit), our survey does not appear to be sensitivity limited for trail detection. Indeed the comets with no detected trails tended to be observed at smaller r . Further, the comets with small q were not preferentially observed at small r (where they would be brighter).

The correlation with orbital shape (q or a) can also be expressed in terms of the Tisserand invariant for Jovian perturbations, T_J . Comets with little interaction with Jupiter (asteroidal or Encke-type orbits, $T_J > 2.94$) have a median $dM/dt = 3.4 \text{ kg s}^{-1}$, while those with $T_J < 2.94$ have a median $dM/dt = 0.8 \text{ kg s}^{-1}$. (A clear outlier is 67P, which is the only low- T_J comet with $dM/dt > 2 \text{ kg s}^{-1}$.) These trends suggest that comets spending more time closer to the Sun may produce more debris, and comets dynamically decoupled from Jupiter may retain debris longer.

The general trend of more-massive trails for comets with smaller q goes somewhat counter to what might be expected from the trend of dust-to-gas ratio being *lower* at smaller q as found in the visible-light survey by A’Hearn et al. (1995). However, if the grains being detected in the inner coma photometry, traced by the scalar $Af\rho$ by A’Hearn et al. (1995) are predominantly small grains, perhaps from fresher surface material, then the new result on debris trails could be explained as an evolution of the *size* of the material ejected from comets. Comets spending more time in the inner Solar System may be dynamically older and more depleted in small particles, while they still appear capable of ejecting larger particles, which build up in their orbits.

For the observations presented in this paper, there is no clear correlation between the

amount of debris in an orbit and the date of last perturbation. Such a correlation would be expected if the perturbations brought comets that were previously in outer-solar-system orbits into $q < 2$ AU orbits, because orbits with $q > 2$ might be expected to have less devolatilized crust. The date of the last significant perturbation was after 1950 for 7 comets: 62P, 65P, 67P, 103P, 111P, 116P, and 120P. Of these, one has a clear non-detection of the trail. It was between 1900 and 1950 for 6 comets (32P, 36P, 69P, 78P, 88P, and 129P). Of these, one has a clear non-detection of the trail. For 17 comets, the strong perturbations occurred before 1900. For the 11 of these relatively stable orbits with detected trails, the average mass production rate is 5.9 kg/s. One of the 17 stable orbits has a clear non-detection of the trail. We also checked whether weaker perturbations due to passing within 1 AU of Jupiter have a significant effect on the amount of material in the near-nuclear trails. Such perturbations are generally minor; they are enough to shift material produced before the perturbation discernibly away from the current projected orbit but not enough to disperse the particles into the zodiacal cloud. (The change in q was typically of order 0.1 AU.) Thus the date of the last strong perturbation does not have a dramatic influence on the amount of debris trail material close to the nucleus, as traced by our *Spitzer* survey. We do expect a significant correlation between T_{pert} and the trail *length*; however, the present observations do not cover enough of each comet’s orbit to show the ends of the trails.

The widths of the debris trails also show some systematic trends. Figure 12 shows the trail width versus the time since perihelion. The trails observed furthest from perihelion (i.e. larger $|T - T_p|$ or r) are wider. If the observations were sensitive to particles emitted within months of the time of observation, the observed trend would be counter to expectations: particles released further from perihelion would be moving slower and would remain closer to the midplane. However if the particles are years old, which we believe to be the case, and they are mostly produced near perihelion, then the width should increase with time

since perihelion:

$$W \propto V_{\perp} |T - T_p|, \quad (11)$$

where V_{\perp} is the component of the ejection velocity perpendicular to the comets' orbits. Gravitational perturbations would further increase the trail width for older particles, but on timescales of multiple orbits. If we interpret the increasing width as due only to ejection velocity, the slope of the trend in Figure 12 yields $V_{\perp} \sim 2 \text{ m s}^{-1}$. Using equation 4, assuming particles are mostly produced near perihelion, with angle ψ relative to the orbit plane, we estimate the particle size

$$\beta \sim \left(\frac{v_{\perp} \cos \psi}{v_1} \right)^2 q(\text{AU}), \quad (12)$$

yielding $\beta \sim 5 \times 10^{-6}$ for a typical perihelion $q \sim 1.5 \text{ AU}$, ejection angle $\psi = 30^\circ$, and $v_1 = 1 \text{ km s}^{-1}$. This size estimate is in accord with the results presented elsewhere in this paper, which show $\beta \ll 10^{-3}$. For the trail width trend to be produced by particles with β as large as 10^{-3} requires $v_1 = 0.07 \text{ km s}^{-1}$, a value too slow to explain the morphology of 2P/Encke's coma (Reach *et al.* 2000) and too low to explain the lengths of trails seen by *IRAS* (Sykes and Walker 1992).

7. Conclusions

The *Spitzer*/MIPS images presented in this paper demonstrate that the production of mm-sized debris is a common feature of Jupiter-family comets: the orbits of most (at least 27 out of the 34 in the present survey) comets are delineated on the sky by 'trails' of mid-infrared emission. The debris trails can only be due to particles with a small ratio of radiation pressure to gravity, $\beta < 10^{-3}$.

The extended surface brightness near Jupiter-family comets contains a mix of particle sizes, $1 < \beta < 10^{-3}$ ($\sim 1\text{--}1000 \mu\text{m}$ for density $\sim 1 \text{ g cm}^{-3}$). Generally, the comae are much brighter in the regions traveled by large particles, bounded by the $10^{-2} < \beta < 10^{-3}$

(100-1000 μm) syndynes, than in the regions traveled by smaller particles. Examples of observations of large-particle-dominated comae include 2P/Encke and 48P/Johnson, for which the viewing geometry allowed straightforward separation of particles of different size.

Dust *tails*, stretching roughly between the anti-solar direction and the $\beta = 1$ syndyne, were detected from some comets, indicating that small particles can also be detected in the mid-infrared images when they are present. Tails are routinely detected for comets observed closest to the Sun. The strong heliocentric and comet-to-comet variety of tails, in contrast to the prevalence and similarity of trails suggests a variation in the dust size distributions—specifically, the ratio of surface area in large versus small particles—among comets. Further work is required to determine whether it is the actual surface area of grains that is varying or the manner in which they are produced (i.e. the velocity distribution or efficiency of fragmentation).

Debris trails are massive, and the inferred mass production rate of mm-sized debris is larger than that of sublimating ice. The predominance of large particles in cometary mass loss agrees with *in situ* spacecraft observations of cometary particles. Green et al. (2004) showed that the mass distribution detected during all three the comet encounters with dust monitors is completely dominated by large particles. We separate the particles into three populations based on the shape of the mass distribution: *small particles*, smaller than 10^{-6} g (size less than 50 μm , $\beta > 10^{-2}$), have a cumulative mass distribution $N(< m) \propto m^{-0.75}$; *intermediate particles* above this mass and until $\sim 10^{-4}$ g (size 250 μm , $\beta \sim 10^{-3}$) have relatively constant cumulative fluence; then for *large particles* the cumulative mass distribution decreases again, approximately as $m^{-0.75}$. Such a size distribution is consistent with the *in situ* observations during the *Giotto* encounter with 1P/Halley (McDonnell et al. 1987) the *Stardust* encounter with 81P/Wild 2 (Green et al. 2004), and interplanetary meteoroids detected by near-Earth spacecraft and meteor magnitudes (Grün *et al.* 1985).

The mass is contained in the largest particles for this size distribution (both overall and within each of the three populations). Within the population of small or large particles, the surface area is contained in the smallest particles. But for the overall distribution, the surface area is dominated by the smallest of the ‘large’ particles, i.e. those with $m \sim 10^{-4}$ g, size $\sim 250 \mu\text{m}$, and $\beta \sim 10^{-3}$.

Figure 13 shows the size distribution weighted by the effective surface area. For $24 \mu\text{m}$ emission, the effective surface area is the cross-sectional area times the absorption efficiency $Q_{24} = (2\pi a/\lambda)$ for $a < \lambda/2\pi$ with $\lambda = 24 \mu\text{m}$. For scattering, $Q = (2\pi a/\lambda)^4$ for $a < \lambda/2\pi$ with $\lambda = 0.55 \mu\text{m}$ for visible light and 1 cm for radar. The efficiencies are all set to unity for $a > \lambda/2\pi$. Using the size distribution observed within the coma of 81P/Wild 2 (Green et al. 2004), the effective surface area for mid-infrared emission is strongly dominated by the particles of $\beta \sim 10^{-3}$, while the effective surface area for visible-light scattering has a significant but not dominant contribution from smaller particles. (Radar backscatter would be produced only by the large particles.) The nature of the size distribution, which is *not a single power law over the range of sizes from micron to cm*, explains why the debris trail observations are dominated by particles with $\beta > 10^{-3}$.

There is an apparent conflict between our interpretation of the mid-infrared images (and the *in situ* size distributions) and the traditional interpretation of optical images and infrared spectra. The optical imaging and infrared spectroscopy studies generally derive particle sizes of order $10 \mu\text{m}$ and consider particles only up to $100 \mu\text{m}$ (cf. Kelley et al. 2006; Lisse et al. 2004; Kolokolova et al. 2004), which all fall within the *small particle* population. The existence of some small particles is required to explain silicate emission features ($a < \lambda/2\pi$ where the silicate feature is at $\lambda \sim 10 \mu\text{m}$). Silicate features have also been correlated with the ‘super-heating’ of grains above the isothermal sphere (blackbody) temperature, due to the lower absorption efficiency of small grains in the infrared where

their cooling occurs ($a < 65/T \mu\text{m}$ where the grain temperature T is in K). Silicate features are generally not strong for Jupiter-family comets, and they can arise from a population of grains distinct from the large particles that dominate the mass loss and produce the debris trails. Figure 13 shows that a significant contribution to mid-infrared emission (and in particular the silicate feature) can arise from the the small particle population if they are significantly hotter than the large grains, even if a large particle population (in excess of the power-law fitted to the small particles) is included. Therefore, we suspect that previous models for coma spectra and optical scattering are sampling only the small particle population; the abundance of large particles such as in meteoroid streams is far larger than would be inferred from an extrapolation of a simple power law normalized to the small particle abundance.

That large particles are produced by most comets is now beyond doubt, but the total mass and the distribution of large particles over comets' orbits remains largely unknown. The present survey only covers the near-nuclear environment, with the debris trails dominated by material from this and the previous revolution. The slow spread of debris trail material, and the rapid influence of gravitational perturbations, spreads debris over a wide area. Strong perturbations by Jupiter occur every $\sim 10^2$ yr for Jupiter-family comets. Comets in the most stable orbits can build up a meteoroid complex, containing many orbits' debris, easily recognizable from surface brightness imaging, while comets suffering recent perturbations will have only young particles in their trails. The debris detected in the present survey with *Spitzer* was faint for most comets, $< 1\%$ of the zodiacal light surface brightness and with a width $< 50''$. Such features are exceptionally difficult to detect in visible light (e.g. Ishiguro et al. 2002) and shallow, wide-area surveys (e.g. *IRAS*). Deeper investigations along the orbits of comets may reveal the extent of their meteoroid complexes and the total mass production of large particles.

The meteoroids of some comets enter the Earth’s atmosphere as meteor showers (Jenniskens 2006). Meteor showers are much more widely dispersed than the debris trails we observed. The debris trails are actually more comparable to the meteor *storms* (Jenniskens 2006; Kresák 1993). The debris trails evolve into the wider meteoroid streams and gradually into the sporadic meteors. The mass of meteoroid streams has been estimated from observed meteor rates, yielding 10^{15-17} g for four well-studied streams (Hughes and McBride 1989). These masses are much larger than those we infer from most debris trails, with the lowest estimated meteoroid stream mass still an order of magnitude larger than the largest estimated debris trail mass. The well-known meteor streams are likely to arise from meteoroids produced by the largest and longest-lived comets that cross the Earth’s orbit. Their properties provide a relatively unique, long-term view of cometary mass loss that is complementary to that obtained from studying debris trails.

The meteoroid mass production rates measured from the present survey has a median 2 kg s^{-1} per comet, with a few undetectable ones having smaller mass-loss. There are ~ 200 known active comets with orbits in the Jupiter family. Assuming the comets we observed are a representative sample, and allowing for as many as 20% having no current meteoroid production (based on the non-detection rate), the total meteoroid input from short-period comets is $\sim 300 \text{ kg s}^{-1}$. The debris trail particles are all on bound orbits, very similar to those of their parent comets—though they will gradually scatter away from their parent comets due to their slightly different initial orbit, non-zero *beta*, different non-gravitational forces due to outgassing and Yarkovsky effect, and different gravitational perturbations by the planets. Thus debris trail particles will gradually fill the inner Solar System. Their lifetime is mostly limited by mutual collisions with other interplanetary particles (Grün *et al.* 1985); the resulting collision products would form via collisional cascade a size distribution including the $\sim 20\text{--}200 \mu\text{m}$ sized particles that generate the zodiacal light (Grün *et al.* 1985; Reach 1988).

Leinert et al. (1983) estimated that the zodiacal cloud loses 600-1000 kg s⁻¹ due to mutual collisions and Poynting-Robertson drag, requiring a corresponding continuous input to maintain the zodiacal light at constant brightness. Constancy of the zodiacal light is not actually required, with the best observational evidence being constancy to $\pm 2\%$ over 11 yr of Helios observations (Leinert et al. 1989). A cometary contribution to the zodiacal cloud may be highly variable, in particular if it were dominated by a few very massive comets soon after injection into a low-perihelion orbit (Napier 2001), or it may be relatively constant if the mass input is relatively evenly distributed among the population of short-period comets as part of their gradual disintegration. It appears, based on the available evidence, that short-period comets lose enough mass to contribute significantly to the interplanetary dust complex. Long-period comets and asteroids almost certainly provide additional contributions.

WTR thanks Giovanni Fazio, who as IRAC Principal Investigator supported part of this project through his Guaranteed Time allotment. This work is based on observations made with the Spitzer Space Telescope, which is operated by the Jet Propulsion Laboratory, California Institute of Technology under a contract with NASA. Support for this work was provided by NASA through an award issued by JPL/Caltech.

REFERENCES

- A'Hearn, M. F., Millis, R. L., Schleicher, D. G., Osip, D. J., and Birch, P. V. 1995. The ensemble properties of comets: Results from narrowband photometry of 85 comets, 1976–1992. *Icarus* 118, 223–270.
- A'Hearn, M.F. et al. 2005. Deep Impact: Excavating Comet Tempel 1. *Science* 310, 258-264.
- Anderson, J. D., Lau, E. L., Bird, M. K., Asmar, S. W., Clark, B. C., Giampieri, G., Gilliland, K. V., and Pätzold, M. 2004. Stardust dynamic science at comet 81P/Wild 2. *JGR* 109, E12S205.
- Brown, M. E., Schaller, E. L., Roe, H. G., Rabinowitz, D. L., Trujillo, C. A. 2006. Direct Measurement of the Size of 2003 UB313 from the Hubble Space Telescope. *ApJ* 643, L61–L63.
- Brown, P., Spalding, R. E., ReVelle, D. O., Tagliaferri, E., and Worden, S. P. 2002. The flux of small near-Earth objects colliding with the Earth. *Nature* 420, 294–296.
- Brownlee, D. E. et al. 2004. Surface of Young Jupiter Family Comet 81P/Wild 2: View from the Stardust Spacecraft. *Science* 304, 1764-1769.
- Burns, J. A., Lamy, P. L., Soter, S. 1979. Radiation forces on small particles in the solar system. *Icarus* 40, .1–48
- Chen, J., and Jewitt, D. 1994. On the rate at which comets split. *Icarus* 108, 265–271.
- Chyba, C. F., Thomas, P. J., Brookshaw, L., Sagan, C. 1990. Cometary Delivery of Organic Molecules to the Early Earth. *Science* 249, 366.
- Chyba, C. F., Thomas, P. J., Zahnle, K. K. 1993. The 1908 Tunguska explosion - Atmospheric disruption of a stony asteroid. *Nature* 361, 40.

- THOMAS, P. J., MCKAY, C. P., CHYBA, C. F. 1996. *Comets and the Origin and Evolution of Life*. Springer, Berlin.
- Delsemme, A. H. 2000. 1999 Kuiper Prize Lecture Cometary Origin of the Biosphere. *Icarus* 146, 313–325.
- Fazio, G. G., 64 colleagues 2004. The Infrared Array Camera (IRAC) for the Spitzer Space Telescope. *ApJS* 154, .10–17
- Fulle, M. 1987. A possible Neck-Line Structure in the dust trail of Comet Halley. *A&A* 181, L13-L14.
- Fulle, M. 1990. Meteoroids from short period comets. *A&A* 230, 220-226.
- Fulle, M. 1996. Dust environment and nucleus spin axis of comet P/Tempel 2 from models of the infrared dust tail observed by IRAS. *A&A* 311, 333-339.
- Goldstein, R., Goldstein, B. E., Balsiger, H., Coates, A. J., Curdt, W. 1991. The composition and plasma signature of a large dust impact on the Giotto spacecraft. *JGR* 96, 13739-13747.
- Green, S. F., McDonnell, J. A. M., McBride, N., Colwell, M. T. S. H., Tuzzolino, A. J., Economou, T. E., Tsou, P., Clark, B. C., Brownlee, D. E. 2004. The dust mass distribution of comet 81P/Wild 2. *JGR* 109, E12S04.
- Grün, E., H. A. Zook, H. Fechtig, and R. H. Giese 1985. Collisional balance of the meteoritic complex. *Icarus* 62, 244–272.
- Hsieh, H. H., Jewitt, D. 2006. A Population of Comets in the Main Asteroid Belt. *Science* 312, 561–563.
- Hughes, D. W., McBride, N. 1989. The mass of meteoroid streams. *MNRAS* 240, 73–79.

- Ishiguro, M., Watanabe, J., Usui, F., Tanigawa, T., Kinoshita, D., Suzuki, J., Nakamura, R., Ueno, M., Mukai, T. 2002. First Detection of an Optical Dust Trail along the Orbit of 22P/Kopff. *ApJ* 572, L117–L121.
- JENNISKENS, P. 2006. *Meteor Showers and their Parent Comets*. Cambridge. 802 pp.
- Jewitt, D., Matthews, H. 1999. Particulate Mass Loss from Comet Hale-Bopp. *AJ* 117, 1056-1062.
- JEWITT, D. 2005. The rise and demise of comets. In: Festou, M. C., Keller, H. U., Weaver, H. A. (Eds.), *Comets II*, Univ. of Arizona Press, Tucson, pp. 659-676.
- Jones, J. 1986. The effect of gravitational perturbations on the evolution of the Taurid meteor stream complex. *MNRAS* 221, 257.
- KELLER, H. U., BRITT, D., BURATTI, B. J., THOMAS, N. 2004. In situ observations of cometary nuclei. In: Festou, M. C., Keller, H. U., Weaver, H. A. (Eds.), *Comets II*, Univ. of Arizona Press, Tucson, pp. 211-222.
- KELLEY, M. S., REACH, W. T., LIEN, D. J. 2007. The dust trail of comet 67P/Churyumov-Gerasimenko, Icarus(submitted).
- Kelley, M. S., Woodward, C. E., Harker, D. E., Wooden, D. H., Gehrz, R. D., Campins, H., Hanner, M. S., Lederer, S. M., Osip, D. J., Pittichova, J., Polomski, E. 2006. A Spitzer Study of Comets 2P/Encke, 67P/Churyumov-Gerasimenko, and C/2001 HT50 (LINEAR-NEAT). *ApJ* 651, 1256-1271.
- Kimura, H., Liu, C.-P. 1975. On the structure of cometary dust tails. *Acta Astron. Sinica* 16, 138-166.
- KOLOKOLOVA, L., HANNER, M. S., LEVASSEUR-REGOURD, A.-CH., GUSTAFSON, B. A. S. 2004. Physical properties of cometary dust from light scattering and

- thermal emission. In: Festou, M. C., Keller, H. U., Weaver, H. A. (Eds.), *Comets II*, Univ. of Arizona Press, Tucson, pp. 577-604.
- Kresák, L. 1993. Cometary dust trails and meteor storms. *A&A* 279, 646.
- KRESÁK, L., KRESÁKOVÁ 1987. The mass loss rates of periodic comets. In: Rolfe, E. J., Battrick, B. (Eds.), *Symposium on the Diversity and Similarity of Comets*, ESA SP-278, Brussels, pp. 739–744.
- Kresák, L., Kresáková 1994. Updating the catalogue of absolute magnitudes of periodic comets. *Plan. Space Sci.* 42, 199-204.
- LAMY, P. L., TOTH, I., FERNANDEZ, Y. R., WEAVER, H. A. 2004. The sizes, shapes, albedos, and colors of cometary nuclei. In: Festou, M. C., Keller, H. U., Weaver, H. A. (Eds.), *Comets II*, Univ. of Arizona Press, Tucson, pp. 223-264.
- Leinert, C., Roser, S., Buitrago, J. 1983. How to maintain the spatial distribution of interplanetary dust. *A&A* 118, 345-357.
- Leinert, C., Pitz, E. 1989. Zodiacal light observed by HELIOS throughout solar cycle no. 21 - Stable dust and varying plasma. *A&A* 210, 399-402.
- Levison, H. F., Duncan, M. J. 1994. The long-term dynamical behavior of short-period comets. *Icarus* 108, 18–36.
- Levison, H. F., Duncan, M. J. 1997. From the Kuiper Belt to Jupiter-Family Comets: The Spatial Distribution of Ecliptic Comets. *Icarus* 127, 13–32.
- Lisse, C. M., M. F. A'Hearn, Y. R. Fernandez, E. Gruen, H. U. Kauff, T. Kostiuk, D.J. Lien, D. J. Osip, S. B. Peschke, R. G. Walker 2004. A tale of two very different comets: ISO and MSX measurements of dust emission from 126P/IRAS (1996) and 2P/Encke (1997). *Icarus* 171, 444–462

- Lowry, S. C., Weissman, P. R. 2003. CCD Observations of distance comets from Steward and Palomar Observatories. *Icarus* 164, 492-503.
- Lowry, S. C., Weissman, P. R., Sykes, M. V., Reach, W. T. 2003. Observations of Periodic Comet 2P/Encke: Physical Properties of the Nucleus and First Visual-Wavelength Detection of Its Dust Trail. Lunar and Planetary Institute Conference Abstracts 34, .2056–
- MAKOVOZ, D., KHAN, I. 2005. Mosaicking with MOPEX. In: P. L. Shopbell, M. C. Britton, R. Ebert (Eds.), *Astronomical Data Analysis Software and Systems XIV*, Astron. Soc. Pacific, San, pp. 1–5. Francisco
- Marsden, B. G., Sekanina, Z. 1974. Comets and nongravitational forces. VI. Periodic comet Encke 1786-1971. *AJ* 79, 413–419.
- MARSDEN, B. G., WILLIAMS, G. V. 2003. *Catalogue of Cometary Orbits 2003: 15th Edition*. Smithsonian Astrophysical Observatory, Cambridge, MA.
- Mazets, E. P. et al. 1987. Dust in Comet P/Halley from VEGA Observations. *A&A* 187, 699-706.
- MEECH, K.J., SVOREN, J. 2004. Using cometary activity to trace the physical and chemical evolution of cometary nuclei. In: Festou, M. C., Keller, H. U., Weaver, H. A. (Eds.), *Comets II*, Univ. of Arizona Press, Tucson, pp. 317-335.
- McDonnell, J. A. M. et al. 1987. The dust distribution within the inner coma of comet P/Halley 1982i - Encounter by Giotto's impact detectors. *A&A* 187, 719-741.
- McDonnell, J. A. M. et al. 1993. Dust particle impacts during the Giotto encounter with Comet Grigg-Skjellerup. *Nature* 362, 732-734.

- Miville-Deschênes, M.-A., Lagache, G. 2005. IRIS: A New Generation of IRAS Maps. *ApJS* 157, 302.
- Napier, W. M. 2001. Temporal variation of the zodiacal dust cloud. *MNRAS* 321, 463-470.
- Pansecchi, L., Fulle, M., Sedmak, G. 1987. The nature of two anomalous structures observed in the dust tail of Comet Bennett 1970. II - A possible Neck-Line Structure. *A&A* 176, 358-366.
- Patzold, M., Edenhofer, P., Bird, M. K., Volland, H. 1993. The Giotto encounter with Comet P/Grigg-Skjellerup - First results from the Giotto Radio-Science Experiment. *A&A* 268, L13-L16.
- PRIALNIK, D., BENKHOFF, J., PODOLAK, M. 2004. Modeling the structure and activity of comet nuclei. In: Festou, M. C., Keller, H. U., Weaver, H. A. (Eds.), *Comets II*, Univ. of Arizona Press, Tucson, pp. 359-387.
- Rabinowitz, D., Scotti, J. 1991. Periodic Comet Faye (1991n). *IAU Circ.* 5366, 3.
- Reach, W. T. 1988. Zodiacal emission. I - Dust near the earth's orbit. *ApJ* 335, 468-485.
- Reach, W. T., M. V. Sykes, D. Lien, and J. K. Davies 2000. The Formation of Encke Meteoroids and Dust Trail. *Icarus* 148, 80-94.
- REACH, W. T., M. S. KELLEY, B. BHATTACHARYA 2007. , in preparation.
- Rieke, G. H., 42 colleagues 2004. The Multiband Imaging Photometer for Spitzer (MIPS). *ApJS* 154, .25-29
- SARUGAKU, Y., ISHIGURO, M., REACH, W. T. 2005. , in preparation.

- Sekanina, Z. 1979. Fan-shaped coma, orientation of rotation axis, and surface structure of a cometary nucleus. I - Test of a model on four comets. *Icarus* 37, 420.
- Sekanina, Z. 1988. Outgassing asymmetry of periodic comet Encke. II - Apparitions 1868-1918 and a study of the nucleus evolution. *Astron. J.* 96, 1455–1475.
- Soderblom, L. A. et al. 2002. Observations of comet 19P/Borrelly by the Miniature Integrated Camera and Spectrometer Aboard Deep Space 1. *Science* 296, 1087-1091.
- Steel, D. I., Asher, D. J., Clube, S. V. M. 1991. The structure and evolution of the Taurid complex. *MNRAS* 251, 632.
- Sykes, M. V. 1993. Great balls of mire. *Nature* 363, 696–697.
- SYKES, M. V., GRÜN, E., REACH, W. T., JENNISKENS, P. 2005. The interplanetary Dust Complex and Comets. In: Festou, M. C., Keller, H. U., and Weaver, H. A. (Eds.), *Comets II*, Tucson, 677–693, pp. Univ. Ariz. Press.
- Sykes, M. V., L. A. Lebofsky, D. M. Hunten, and F. J. Low 1986. The discovery of dust trails in the orbits of periodic comets. *Science* 232, 1115–1117.
- Sykes, M. V., D. J. Lien, and R. G. Walker 1990. The Tempel 2 dust trail. *Icarus* 86, 236–247.
- Sykes, M. V., and R. G. Walker 1992. Cometary dust trails. I. Survey. *Icarus* 95, 180–210.
- Turco, R. P., Toon, O. B., Park, C., Whitten, R. C., Pollack, J. B., Noerdlinger, P. 1982. An analysis of the physical, chemical, optical, and historical impacts of the 1908 Tunguska meteor fall. *Icarus* 50, 1–52.

- Vaubailon, J., Colas, F., Jorda, L. 2005. A new method to predict meteor showers. I. Description of the model. *A&A* 439, 751–760.
- Weismann, P. R., Lowry, S. C. 2003. The Size Distribution of Jupiter-Family Cometary Nuclei. *LPI* 34, 2003;2003.
- Whipple, F. L. 1950. A comet model. I. The acceleration of Comet Encke. *Astrophys. J.* 111, 375–394.
- Whipple, F. L. 1951. A comet model. II. Physical relations for comets and meteors. *Astrophys. J.* 113, 464–474.
- Whipple, F. L. 1955. A comet model. III. The zodiacal light. *ApJ* 121, 750–770.
- YEOMANS, D. 1991. *Comets: A Chronological History of Observation, Science, Myth, and Folklore*. Wiley, New York, 485 pp.

Table 1. Spitzer Comet Trail Survey Summary

Comet	Date	UT (hh:mm)	$T - T_p$ (days)	R (AU)	Δ (AU)	q (AU)	e	T_J	T_{pert}^a	PA_{Sun} ($^\circ$)	PA_{trail} ($^\circ$)	F_ν^b (mJy)	dM_3/dt^c (kg s^{-1})	Trail type ^d
2P/Encke	06/20/04	18:35	173	2.53	2.02	0.339	0.847	3.02	<1769	70.4	211.1	69	26	long L F
4P/Faye	10/02/2006	2:29	-44	1.73	0.98	1.67	0.567	2.75	1816	75.9	264.2	7400	1	narrow L F
9P/Tempel 1	03/14/04	15:02	-478	3.75	3.40	1.502	0.633	2.97	<1839	272.6	259.3	0.77	14	common F
10P/Tempel 2	07/08/04	10:12	-222	2.49	2.34	1.468	0.526	2.96	<1846	292.4	287.8	0.60	26	long L F
32P/Comas Sola	01/26/05	14:28	-66	1.93	1.36	1.834	0.569	2.67	1912	253.1	233.6	1811	0.8	narrow F
36P/Whipple	01/22/04	10:43	199	3.24	2.79	3.088	0.259	2.95	1922	251.4	261.6	30.2	8.1	intermed F
42P/Neujmin 3	10/13/04	17:25	89	2.17	1.54	2.018	0.584	2.63	1850	254.7	258.9	120	...	none
48P/Johnson	10/13/04	21:12	1	2.31	1.94	2.310	0.365	2.94	<1903	256.0	274.1	533	2.6	narrow L F
49P/Arend-Rigaux	12/05/04	13:40	-82	1.64	0.99	1.367	0.612	2.71	<1801	236.4	270.0	1497	...	none
53P/van Biesbroeck	08/06/04	12:26	302	3.94	3.30	2.415	0.551	2.65	1850	69.8	252.5	154	...	(tail)
56P/Slaughter-Burnham	12/02/04	03:47	-44	2.56	1.98	2.530	0.504	2.71	<1800	248.0	236.7	217	1.8	narrow L F
62P/Tsuchinshan 1	02/03/05	21:50	57	1.61	0.96	1.491	0.577	2.79	1960	99.2	300.8	929	1.0	narrow F
65P/Gunn	08/21/04	22:58	467	3.51	2.97	2.447	0.318	2.99	1965	76.4	239.0	188	11	long L
67P/Chury-Ger	02/23/04	03:42	554	4.47	4.05	1.292	0.631	2.74	1959	106.6	296.8	8.6	31	narrow L F
69P/Taylor	12/03/04	15:20	2	1.94	1.38	1.943	0.467	2.81	1925	107.0	262.5	200	0.3	narrow L
71P/Clark	04/11/05	10:54	-422	3.48	3.00	1.559	0.500	2.99	<1945	285.2	278.2	1.8	4.9	debris L F
71P/Clark(epoch2)	06/09/2006	19:18	3	1.56	0.84	1.56	0.50	2.99	<1945	77.2	269.9	5100	2	narrow L
78P/Gehrels 2	09/21/04	15:05	-36	2.03	1.32	2.004	0.463	2.88	1911	74.8	261.8	2400	1.3	narrow L
88P/Howell	08/27/04	05:37	136	1.96	1.47	1.388	0.556	2.94	1907	74.3	243.5	704	2.3	narrow L
94P/Russell 4	03/14/04	16:26	198	2.60	2.18	2.229	0.364	3.00	<1895	98.4	287.6	45.1	9.9	intermed F
103P/Hartley 2	01/25/05	08:25	252	2.95	2.46	1.033	0.700	2.64	1982	122.8	273.7	67.9	...	(tail)
104P/Kowal 2	03/05/05	15:29	300	3.06	2.45	1.395	0.585	2.80	<1894	126.9	272.4	3.4	2.1	intermed F
107P/Wilson-Harrington	07/10/04	09:51	370	3.3	3.10	1.001	0.621	3.08	<1915	2.4	...	none

Table 1—Continued

Comet	Date	UT (hh:mm)	$T - T_p$ (days)	R (AU)	Δ (AU)	q (AU)	e	T_J	T_{pert}^a	PA_{Sun} ($^\circ$)	PA_{trail} ($^\circ$)	F_ν^b (mJy)	dM_3/dt^c (kg s $^{-1}$)	Trail type ^d
108P/Ciffreo	10/05/2006	14:30	-284	2.97	2.35	1.71	0.542	2.77	<1948	249.2	271.8	3.2	0.2	narrow L F
111P/Helin-Roman-Croc	11/09/04	22:26	-45	3.48	3.01	3.477	0.140	3.02	1976	98.0	273.9	1.4	1.8	narrow F
116P/Wild 4	06/23/04	05:21	518	3.71	3.13	2.166	0.377	3.00	1987	71.9	246.3	28.4	...	(tail)
120P/Mueller 1	09/17/04	10:36	-13	2.75	2.09	2.743	0.337	2.91	1957	69.4	246.8	14.2	2.1	narrow L F
121P/Shoemaker-Holt 2	12/31/04	05:18	120	2.75	2.17	2.651	0.338	2.87	<1915	102.0	282.1	398		(tail)
123P/West-Hartley	01/22/04	05:31	44	2.16	1.71	2.130	0.447	2.83	<1892	107.7	311.1	825	0.8	narrow L
127P/Holt-Olmstead	02/20/04	21:13	253	2.74	2.24	2.158	0.368	2.98	<1805	267.8	256.6	7.4	4.2	intermed F
129P/Shoemaker-Levy 3	03/03/05	05:37	-94	2.85	2.30	2.811	0.249	3.02	1914	267.6	271.6	74	4.9	long L F
131P/Mueller 2	12/22/04	05:35	4	2.42	1.87	2.419	0.343	2.98	1785	245.8	255.3	36	0.3	narrow F _{CT}
133P/Elst-Pizarro	04/11/05	08:11	-811	3.59	3.04	2.63	0.165	3.18	<1945	115.5	292.1	4.7	0.1:	narrow F _{faint}
141P/Machholz 2	08/22/04	09:54	189	2.53	2.21	0.749	0.751	2.71	<1968	281.5	252.9	2.5	...	debris L F
P/2003 S2	12/03/04	16:00	453	3.59	3.03	2.457	0.358	2.94	1850	101.7	278.2	4.8	2.6	narrow F

^aYear of last significant orbital perturbation

^bFlux within 12.5" aperture centered on nucleus

^cMass production rate of trail particles assumed to have $\beta = 10^{-3}$, $\rho = 1 \text{ g cm}^{-3}$

^d=leading, F=following nucleus; 'long' means the trail extends to the edge of the image; '(tail)' means the small-particle dust tail dominates the image preventing debris trail detection; 'intermed' means the trail follows the $\beta = 10^{-3}$ syndyne more closely than it follows the projected orbit of the nucleus.

Table 2. Debris trail brightnes profile fits^a

ϕ (")	$\phi\Delta$ (10^4 km)	I_ν (MJy/sr)	τ (10^{-9})	W (")	$W\Delta$ (10^4 km)	F_{1D} (mJy/')	$dM_3/d\phi$ (10^{10} g/deg)
2P/Encke							
323	47.1	0.71	5.4	54.3	7.9	54.12	135.0
248	36.1	0.81	6.2	54.5	8.0	62.44	155.6
173	25.2	0.93	7.1	45.1	6.6	59.15	147.3
-128	-18.6	0.78	5.9	29.4	4.3	32.35	80.6
-203	-29.6	0.87	6.6	43.0	6.3	52.69	131.4
-278	-40.5	0.75	5.7	42.4	6.2	44.94	111.9
-353	-51.5	0.65	5.0	46.1	6.7	42.46	105.7
4P/Faye							
446	31.8	0.27	1.2	51.4	3.7	13.9	6.5
295	21.1	0.24	1.1	66.1	4.7	16.0	7.7
9P/Tempel 1							
-312	-76.7	0.14	2.1	30.1	7.4	5.79	81.8
-463	-113.5	0.15	2.3	50.5	12.4	10.67	150.8
10P/Tempel 2							
475	82.4	0.35	2.6	43.2	7.5	21.58	69.9

Table 2—Continued

ϕ (")	$\phi\Delta$ (10^4 km)	I_ν (MJy/sr)	τ (10^{-9})	W (")	$W\Delta$ (10^4 km)	F_{1D} (mJy/')	$dM_3/d\phi$ (10^{10} g/deg)
400	69.4	0.32	2.4	34.7	6.0	15.88	51.4
325	56.4	0.34	2.5	32.8	5.7	15.60	50.5
250	43.4	0.39	2.8	35.4	6.1	19.21	62.3
175	30.4	0.39	2.9	28.3	4.9	15.41	50.0
100	17.4	0.47	3.5	26.6	4.6	17.58	57.0
-125	-21.7	0.62	4.6	32.0	5.6	27.94	90.5
-200	-34.7	0.65	4.8	31.7	5.5	28.81	93.5
-275	-47.7	0.64	4.8	28.5	4.9	25.86	83.9
-350	-60.8	0.67	5.0	30.0	5.2	28.49	92.4
-425	-73.8	0.70	5.2	36.9	6.4	36.45	118.0
-500	-86.8	0.73	5.4	38.6	6.7	39.83	129.0
32P/Comas Sola							
-543	-53.3	0.05	0.2	18.6	1.8	1.22	0.9
-992	-97.5	0.06	0.3	35.4	3.5	2.96	2.2
36P/Whipple ^b							
-123	-24.7	0.12	1.4	50.8	10.3	8.59	62.4
-197	-39.9	0.09	1.0	34.4	6.9	4.19	30.3
-273	-55.1	0.08	1.0	34.3	6.9	4.07	29.5
-350	-70.7	0.08	1.0	49.7	10.0	5.87	42.5

Table 2—Continued

ϕ (")	$\phi\Delta$ (10^4 km)	I_ν (MJy/sr)	τ (10^{-9})	W (")	$W\Delta$ (10^4 km)	F_{1D} (mJy/')	$dM_3/d\phi$ (10^{10} g/deg)
48P/Johnson							
400	53.4	0.06	0.4	22.2	3.0	1.86	3.7
325	43.4	0.07	0.4	35.5	4.7	3.39	6.7
250	33.3	0.08	0.5	33.0	4.4	3.73	7.4
175	23.3	0.09	0.6	30.3	4.0	3.86	7.7
-125	-16.7	0.09	0.6	15.3	2.0	1.89	3.7
-200	-26.7	0.13	0.8	24.3	3.2	4.41	8.7
-275	-36.7	0.15	1.0	13.6	1.8	2.79	5.5
-350	-46.7	0.13	0.9	21.5	2.9	4.03	7.9
-425	-56.7	0.19	1.2	16.2	2.2	4.27	8.4
-500	-66.7	0.16	1.1	15.8	2.1	3.62	7.2
56P/Slaughter-Burnham							
317	45.6	0.03	0.3	27.4	3.9	1.35	3.3
-282	-40.6	0.04	0.3	27.9	4.0	1.59	3.9
-432	-62.2	0.04	0.3	15.1	2.2	0.91	2.2
-582	-83.7	0.05	0.4	21.8	3.1	1.61	3.9
-732	-105.3	0.07	0.5	33.4	4.8	3.07	7.4
-882	-126.8	0.05	0.4	27.7	4.0	2.11	5.1
-1032	-148.4	0.03	0.3	15.8	2.3	0.76	1.8
62P/Tsuchinshan 1							

Table 2—Continued

ϕ (")	$\phi\Delta$ (10^4 km)	I_ν (MJy/sr)	τ (10^{-9})	W (")	$W\Delta$ (10^4 km)	F_{1D} (mJy/')	$dM_3/d\phi$ (10^{10} g/deg)
148	10.1	0.07	0.3	78.0	5.3	7.78	2.2
65P/Gunn							
395	82.9	0.09	1.3	35.9	7.5	4.80	45.9
320	67.1	0.14	1.9	51.4	10.8	10.00	95.3
245	51.5	0.10	1.4	39.7	8.3	5.70	54.3
67P/Churyumov-Gerasimenko							
400	117.9	0.05	1.1	25.6	7.5	1.88	54.1
325	95.8	0.05	1.2	30.3	8.9	2.28	65.5
250	73.7	0.05	1.1	29.7	8.8	2.07	59.2
175	51.6	0.07	1.5	27.4	8.1	2.73	78.6
-200	-59.0	0.39	8.6	25.2	7.4	13.98	401.1
-275	-81.1	0.30	6.6	27.0	8.0	11.58	332.4
-350	-103.2	0.27	5.8	30.6	9.0	11.49	329.5
-425	-125.3	0.22	4.8	35.7	10.5	11.03	316.8
-500	-147.4	0.21	4.5	51.5	15.2	15.01	431.1
69P/Taylor							
583	57.9	0.04	0.2	13.8	1.4	0.85	0.7

Table 2—Continued

ϕ (")	$\phi\Delta$ (10^4 km)	I_ν (MJy/sr)	τ (10^{-9})	W (")	$W\Delta$ (10^4 km)	F_{1D} (mJy/')	$dM_3/d\phi$ (10^{10} g/deg)
357	35.5	0.04	0.2	17.0	1.7	0.97	0.8
71P/Clark							
90	19.6	0.07	0.9	20.9	4.5	2.10	20.1
-60	-13.0	0.07	1.0	22.7	4.9	2.37	22.7
-135	-29.3	0.08	1.1	31.1	6.8	3.47	33.3
-285	-61.9	0.12	1.5	27.3	5.9	4.44	42.5
-360	-78.2	0.10	1.3	28.5	6.2	4.00	38.2
-435	-94.5	0.10	1.3	26.9	5.8	3.86	36.9
-510	-110.8	0.11	1.5	29.6	6.4	4.77	45.5
-585	-127.1	0.12	1.5	28.5	6.2	4.64	44.5
-660	-143.4	0.11	1.4	32.2	7.0	4.94	47.3
-735	-159.7	0.13	1.7	26.1	5.7	4.85	46.3
-810	-176.0	0.10	1.4	33.3	7.2	4.91	47.2
78P/Gehrels 2							
323	31.0	0.18	1.0	19.5	1.9	4.92	3.7
285	27.4	0.16	0.9	11.7	1.1	2.63	2.0
135	13.0	0.18	0.9	18.7	1.8	4.64	3.5
88P/Howell							

Table 2—Continued

ϕ (")	$\phi\Delta$ (10^4 km)	I_ν (MJy/sr)	τ (10^{-9})	W (")	$W\Delta$ (10^4 km)	F_{1D} (mJy/')	$dM_3/d\phi$ (10^{10} g/deg)
437	44.8	0.12	0.6	47.2	4.8	7.91	7.0
288	29.5	0.11	0.6	27.1	2.8	4.25	3.8
94P/Russell 4 ^b							
-125	-20.0	0.46	3.7	22.1	3.5	14.41	43.3
-275	-43.9	0.21	1.7	28.5	4.5	8.60	25.9
-500	-79.8	0.09	0.7	18.3	2.9	2.23	6.7
104P/Kowal 2 ^b							
-223	-39.6	0.06	0.6	31.7	5.6	2.50	12.6
-373	-66.3	0.03	0.3	24.0	4.3	1.07	5.4
108P/Ciffreo							
-403	-68.7	0.05	1.33	11.1	1.9	0.8	0.1
-283	-48.2	0.05	1.20	11.1	1.9	0.7	0.1
-204	-34.8	0.07	1.71	13.2	2.3	1.3	0.1
111P/Helin-Roman-Crockett							
-170	-36.9	0.04	0.5	22.1	4.8	1.18	11.3
-320	-69.5	0.05	0.7	15.8	3.4	1.10	10.7

Table 2—Continued

ϕ (")	$\phi\Delta$ (10^4 km)	I_ν (MJy/sr)	τ (10^{-9})	W (")	$W\Delta$ (10^4 km)	F_{1D} (mJy/')	$dM_3/d\phi$ (10^{10} g/deg)
-470	-102.0	0.05	0.6	21.9	4.8	1.43	13.6
120P/Mueller 1							
443	67.1	0.04	0.3	13.3	2.0	0.76	2.3
293	44.4	0.03	0.3	12.0	1.8	0.51	1.6
143	21.6	0.02	0.2	12.3	1.9	0.37	1.1
-120	-18.2	0.11	0.9	20.6	3.1	3.12	9.5
-195	-29.6	0.06	0.6	13.9	2.1	1.25	3.8
-270	-40.9	0.04	0.3	21.2	3.2	1.20	3.7
-345	-52.3	0.08	0.7	20.2	3.1	2.39	7.3
-420	-63.7	0.07	0.7	16.5	2.5	1.74	5.3
123P/West-Hartley							
425	52.8	0.04	0.2	25.4	3.2	1.46	2.0
127P/Holt-Olmstead ^b							
-127	-20.7	0.10	0.9	40.7	6.6	5.71	19.9
-203	-33.0	0.06	0.5	31.6	5.1	2.59	9.1
129P/Shoemaker-Levy 3							

Table 2—Continued

ϕ (")	$\phi\Delta$ (10^4 km)	I_ν (MJy/sr)	τ (10^{-9})	W (")	$W\Delta$ (10^4 km)	F_{1D} (mJy/')	$dM_3/d\phi$ (10^{10} g/deg)
430	71.8	0.14	1.3	31.2	5.2	5.96	23.4
355	59.3	0.12	1.1	32.3	5.4	5.42	21.2
280	46.7	0.18	1.6	21.5	3.6	5.33	21.0
205	34.2	0.16	1.5	23.4	3.9	5.39	21.1
130	21.7	0.16	1.5	20.0	3.3	4.64	18.2
-170	-28.4	0.37	5.77	21.9	3.7	11.52	25.23
-245	-40.9	0.38	5.91	19.4	3.2	10.42	22.81
-320	-53.4	0.36	5.57	19.4	3.2	9.85	21.58
-395	-65.9	0.30	4.66	20.8	3.5	8.82	19.32
-470	-78.5	0.25	3.90	19.9	3.3	7.06	15.45
-545	-91.0	0.24	3.66	23.8	4.0	7.93	17.36
-620	-103.5	0.24	3.77	27.8	4.6	9.55	20.92
-695	-116.0	0.25	3.86	27.0	4.5	9.49	20.78
-770	-128.5	0.23	3.63	22.9	3.8	7.59	16.63
-845	-141.1	0.22	3.39	25.7	4.3	7.92	17.35
-920	-153.6	0.19	3.01	27.5	4.6	7.54	16.52
-995	-166.1	0.21	3.30	35.7	6.0	10.73	23.51
-1070	-178.6	0.21	3.21	33.5	5.6	9.81	21.48
131P/Mueller 2							
-318	-43.2	0.04	0.3	6.5	0.9	0.40	0.8

P/2003 S2

Table 2—Continued

ϕ (")	$\phi\Delta$ (10^4 km)	I_ν (MJy/sr)	τ (10^{-9})	W (")	$W\Delta$ (10^4 km)	F_{1D} (mJy/')	$dM_3/d\phi$ (10^{10} g/deg)
-183	-40.1	0.09	1.2	16.7	3.7	2.06	21.3
-258	-56.6	0.04	0.5	15.5	3.4	0.82	8.4
-333	-73.0	0.04	0.5	9.1	2.0	0.46	4.7
-408	-89.5	0.03	0.4	17.1	3.7	0.75	7.8

^a ϕ is the distance behind the nucleus at which the trail profile was analyzed. F_{1D} is the brightness integrated perpendicular to the trail. $dM_3/d\phi$ is the mass per unit projected angle on the sky.

^bProfiles taken through map rotated at angle of $\beta = 10^{-3}$ syndyne rather than $\beta = 0$, to match observed orientation of trail.

Table 3. Mass-loss rates from visible observations

Comet	Q_{max} (10^{28} mol s $^{-1}$)	^a $\langle Q \rangle / Q_{max}$	dM_{ice}/dt (kg s $^{-1}$)	dM/dt (K&K) (kg s $^{-1}$)
2P/Encke	4.6	0.014	19	71
9P/Tempel 1	1.7	0.20	96	2.7
10P/Tempel 2	0.2	0.14	9.1	6.2
49P/Arend-Rigaux	0.18	0.074	3.8	0.8
62P/Tsuchinshan 1	0.26	0.12	9.4	0.4
67P/Chury-Ger	0.41	0.057	6.7	1.1
65P/Gunn	0.3	0.25	22	5.6
69P/Taylor	0.14	0.19	7.7	1.8
78P/Gehrels 2	0.025	0.17	1.2	1.6
88P/Howell	0.24	0.14	9.5	1.8
94P/Russell 4	0.11	0.23	7.5	3.2

^afrom A’Hearn et al. (1995), Table III last column; except for 65P/Gunn for which we scaled Q(OH) from its observed distance to perihelion $d\theta/d\phi$ is the change in mean anomaly per unit degree on the sky.

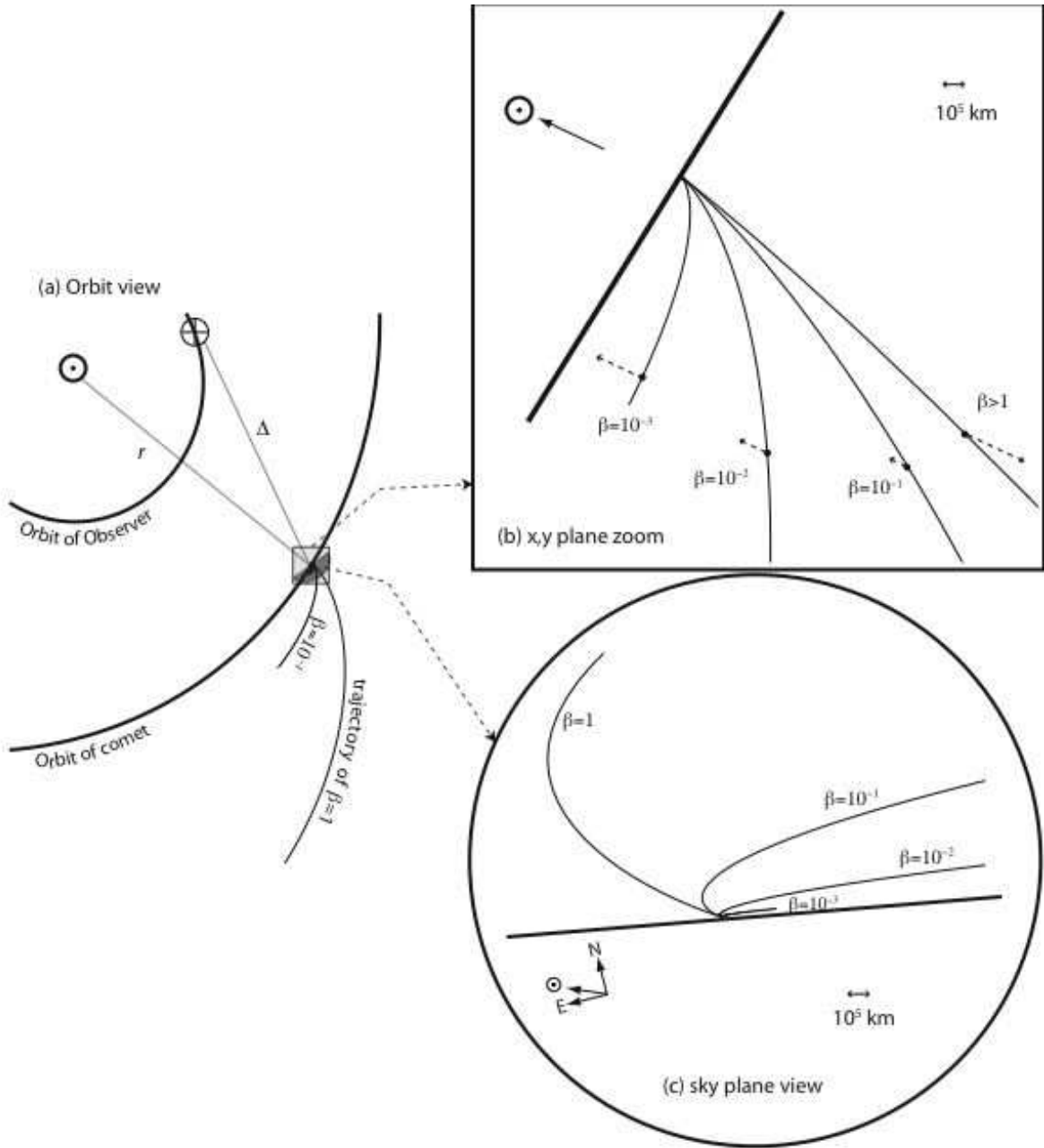


Fig. 1.— Illustration of cometary debris dynamics and viewing geometry, drawn specifically for the conditions of the observation of 48P/Johnson. (a) In a view looking down onto the ecliptic plane, the orbits of the observatory and comet are shown together with the vectors from comet-to-Sun and comet-to-observatory. The trajectory of particles with $\beta = 1$ (radiation pressure equal to gravitational force) and $\beta = 0.1$ are shown as thin arcs stretching away from the comet. (b) This is a blow-up of the region in panel (a) shown as a light-grey square. The trajectories of particles with a range of β (ratio of radiation pressure to gravity) are shown as thin arcs, and the orbit of the comet as a thick line. Dashed vectors on each syndyne show the net direction of solar forces, which is repulsive for $\beta > 1$ and progressively more attractive as $\beta \rightarrow 0$. (c) This panel shows a view projected onto the plane of the sky, perpendicular to the observer-comet vector. The projected trajectories from panel (b) are shown; these are the *zero-velocity syndynes*, which serve as a guide to cometary dust and debris. The smallest particles (largest β) feel the most radiation pressure, and they lie closer to the antisolar direction or $\beta = 1$ syndyne. Progressively larger particles lie closer to the comet’s projected orbit, and particles with $\beta < 10^{-3}$ are effectively along the orbit and form the *debris trails* which are the focus of the present survey.

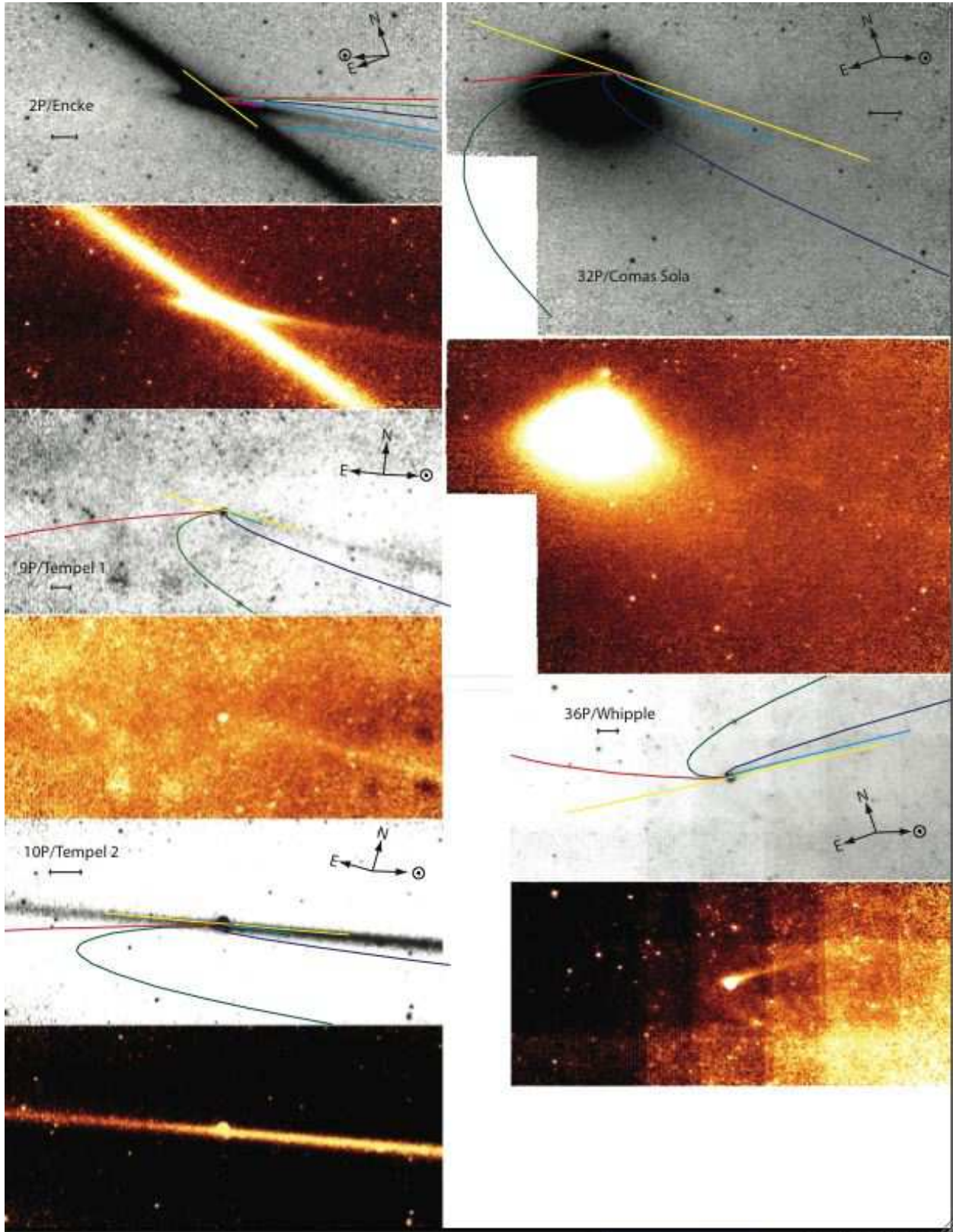


Fig. 2.— Mid-infrared images and zero-velocity syndynes for comets 2P/Encke, 9P/Tempel 1, 10P/Tempel 2, 32P/Comas Sola, and 36P/Whipple. For each comet there are two panels. The upper, labeled panel shows the $24\ \mu\text{m}$ image in greyscale together with the image orientation (celestial N and E), a scale bar showing 10^5 km perpendicular to the line of sight, the projected orbit (yellow line), and color-coded syndynes that show the location of particles of different size emitted over the 1 yr period before observation (red, green, blue, cyan, and magenta correspond to $\beta = 1, 10^{-1}, 10^{-2}, 10^{-3}, 10^{-4}$, where β is the ratio of radiation to gravitational force and is approximately the inverse of the particle size in μm). For each comet, the lower panel shows the mid-infrared image alone, in a color table that ranges from black (faintest) through shades of orange to white (brightest).

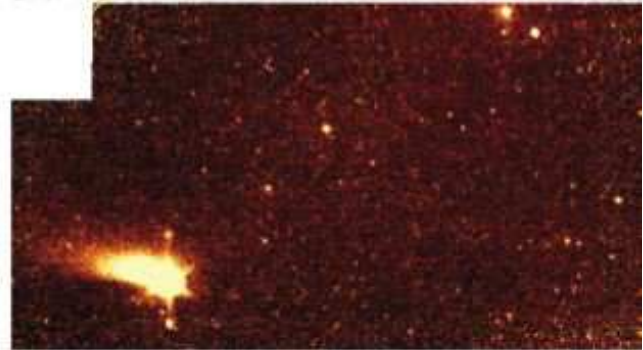
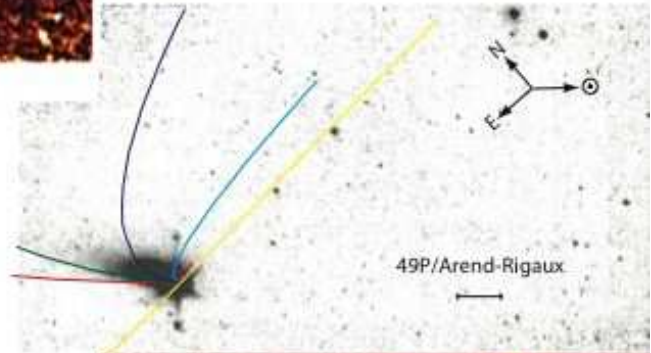
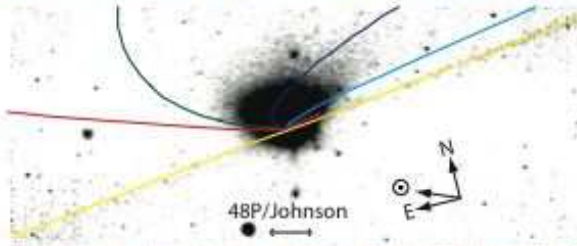
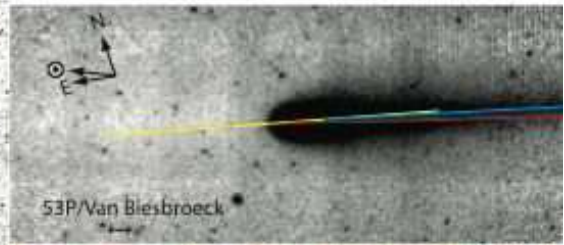
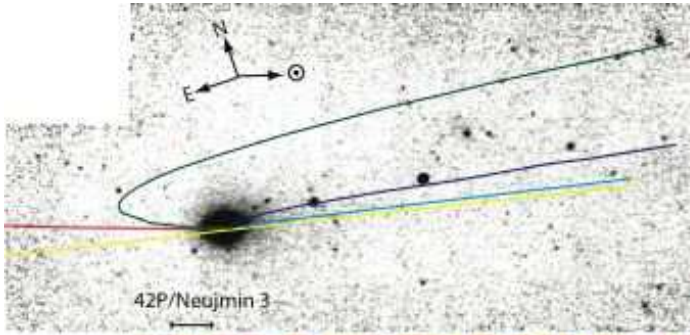


Fig. 3.— Mid-infrared images and zero-velocity syndynes for comets 42P/Neujmin 3, 48P/Johnson, 53P/van Biesbroeck, and 49P/Arend-Rigaux. Labels and overlays are the same as in Figure 2. The color images of 42P and 49P have been convolved with a 3-pixel ($2.5''/\text{pixel}$) gaussian.

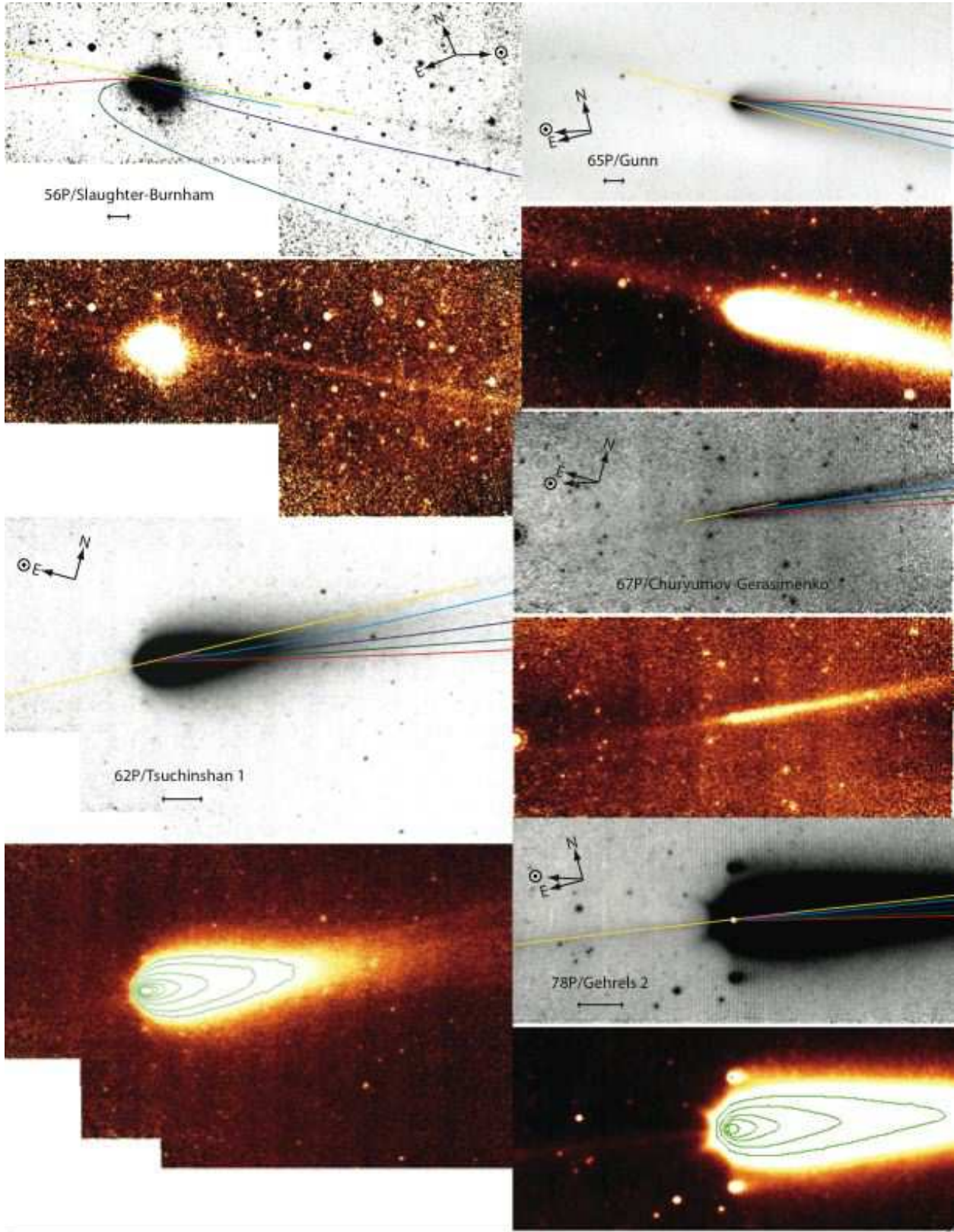


Fig. 4.— Mid-infrared images and zero-velocity syndynes for comets 56P/Slaughter-Burnham, 62P/Tsuchinshan 1, 65P/Gunn, 67P/Churyumov-Gerasimenko, and 78P/Gehrels 2. Labels and overlays are the same as in Figure 2. For 62P, the color table runs from 37.7–41 MJy sr⁻¹ (linear) and the contours from 39.5–70 MJy sr⁻¹ (square-root spaced). The Sun was almost directly E of 62P at the time of observation. For 78P, the color table runs from 41.1–43.6 MJy sr⁻¹ (linear) and the contours from 45–100 MJy sr⁻¹ (square-root spaced). The two bright splotches 1/3 of the image above and below 78P are latent images of the nucleus (which saturated the detector) and inner coma.

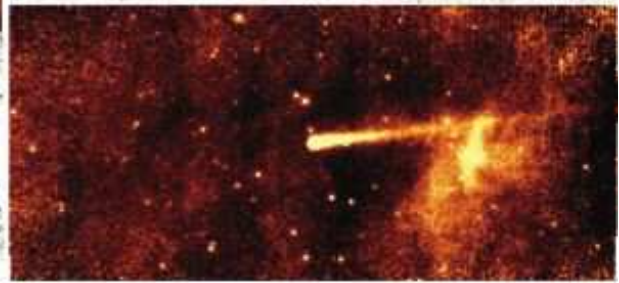
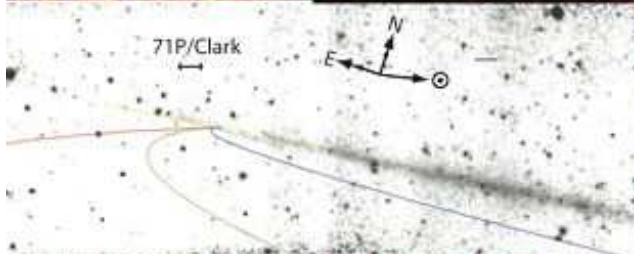
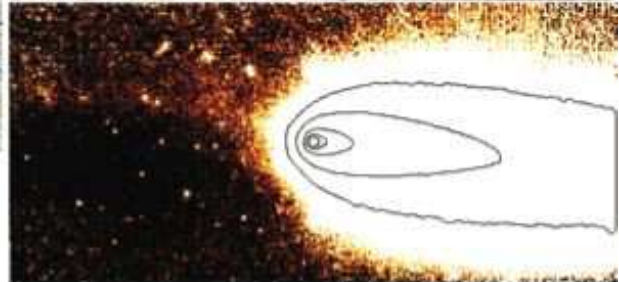
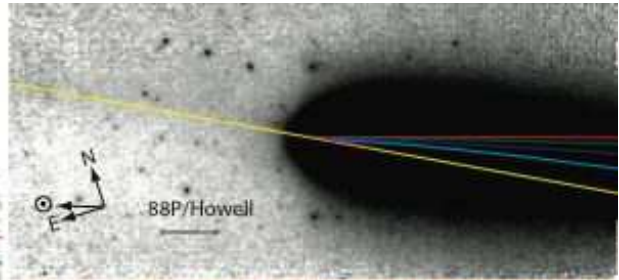
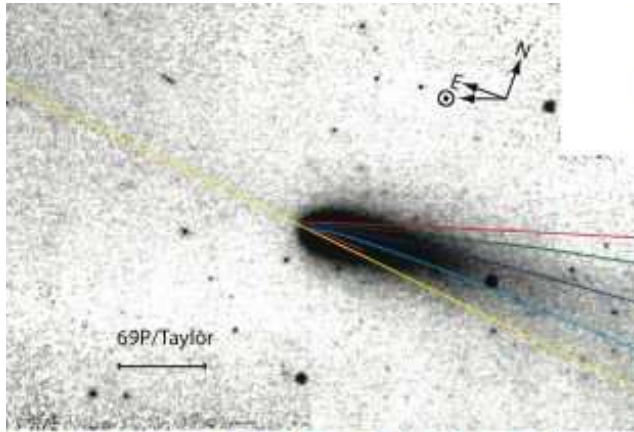


Fig. 5.— Mid-infrared images and zero-velocity syndynes for comets 69P/Taylor, 71P/Clark, 88P/Howell, and 94P/Russell 4. Labels and overlays are the same as in Figure 2. The color image of 69P was convolved with a 2-pixel radius tophat filter.

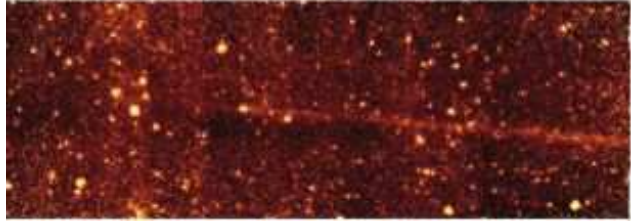
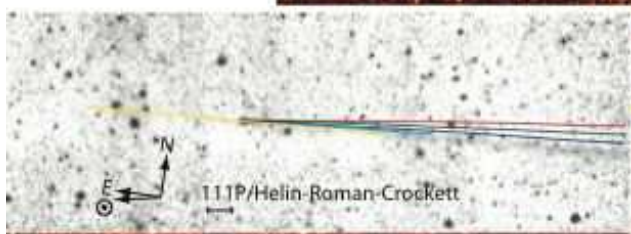
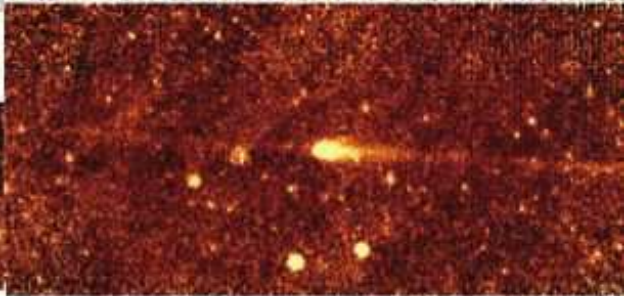
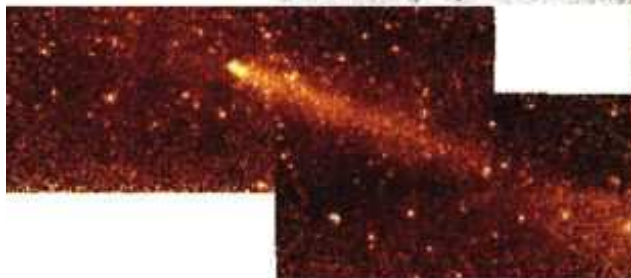
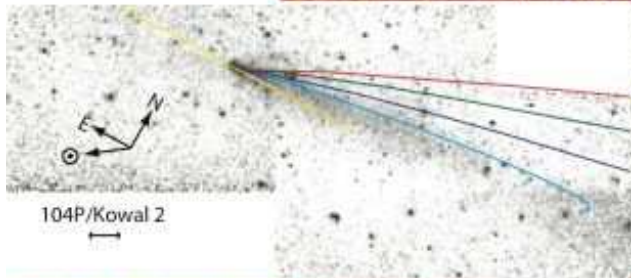
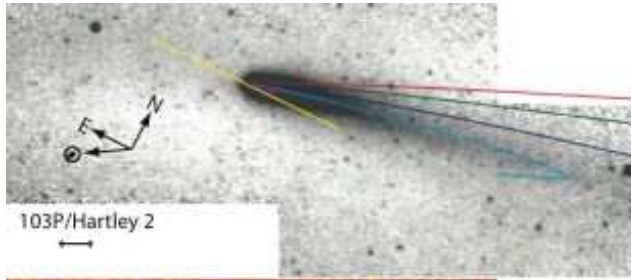


Fig. 6.— Mid-infrared images and zero-velocity syndynes for comets 103P/Hartley 2, 104P/Kowal 2, 111P/Helin-Roman-Crockett, 116P/Wild 4, 120P/Mueller 1, and 121P/Shoemaker-Holt 2. Labels and overlays are the same as in Figure 2.

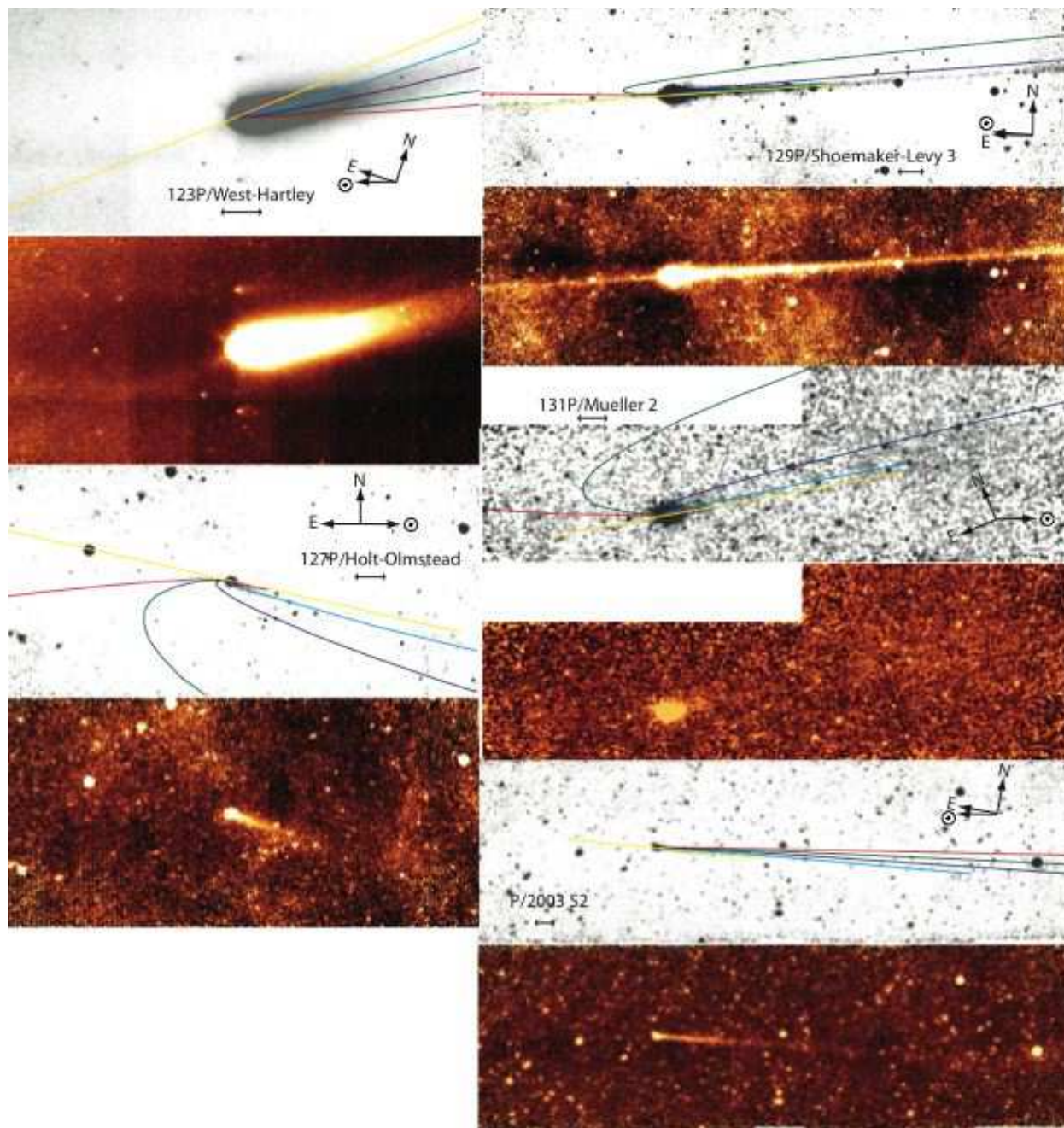


Fig. 7.— Mid-infrared images and zero-velocity syndynes for comets 123P/West-Hartley, 127P-Holt-Olmstead, 129P/Shoemaker-Levy 3, 131P/Mueller 2, and P/2003 S2. Labels and overlays are the same as in Figure 2. For 131P, the images were smoothed with a 2 pixel radius tophat.

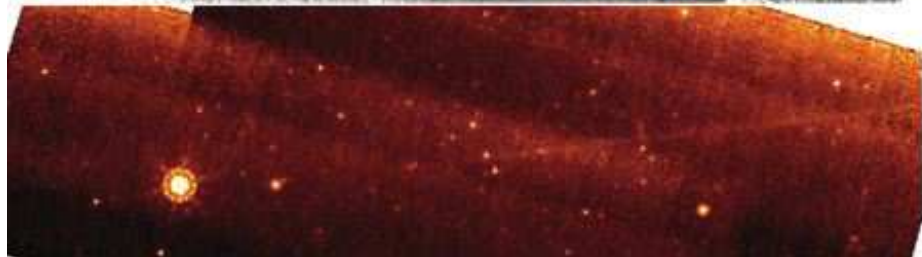
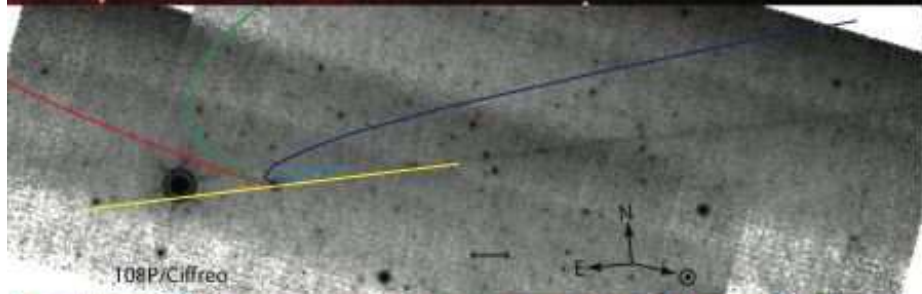
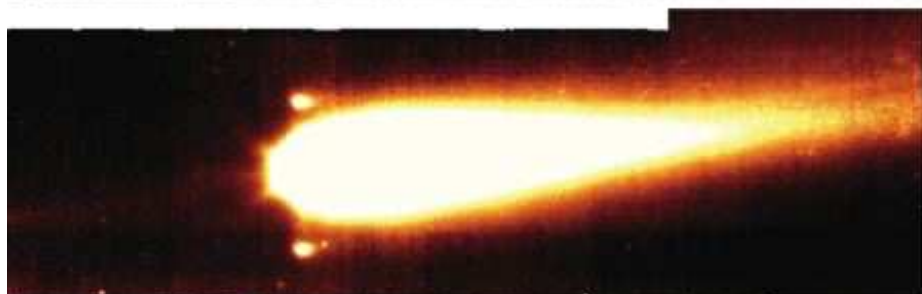
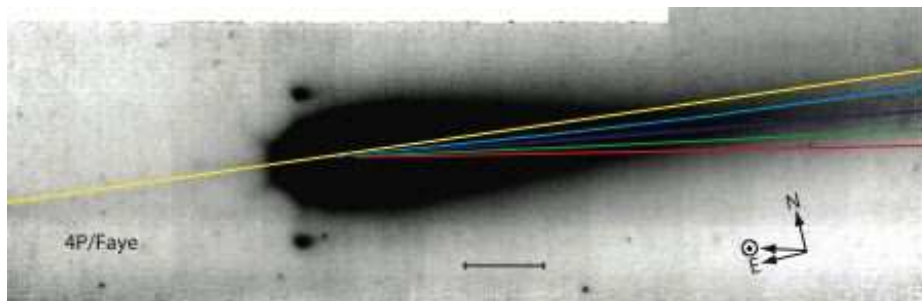


Fig. 8.— Mid-infrared images and zero-velocity syndynes for comets 4P/Faye, 108P/Cifreio, and 71P/Clark from 2006 observations. Labels and overlays are the same as in Figure 2.

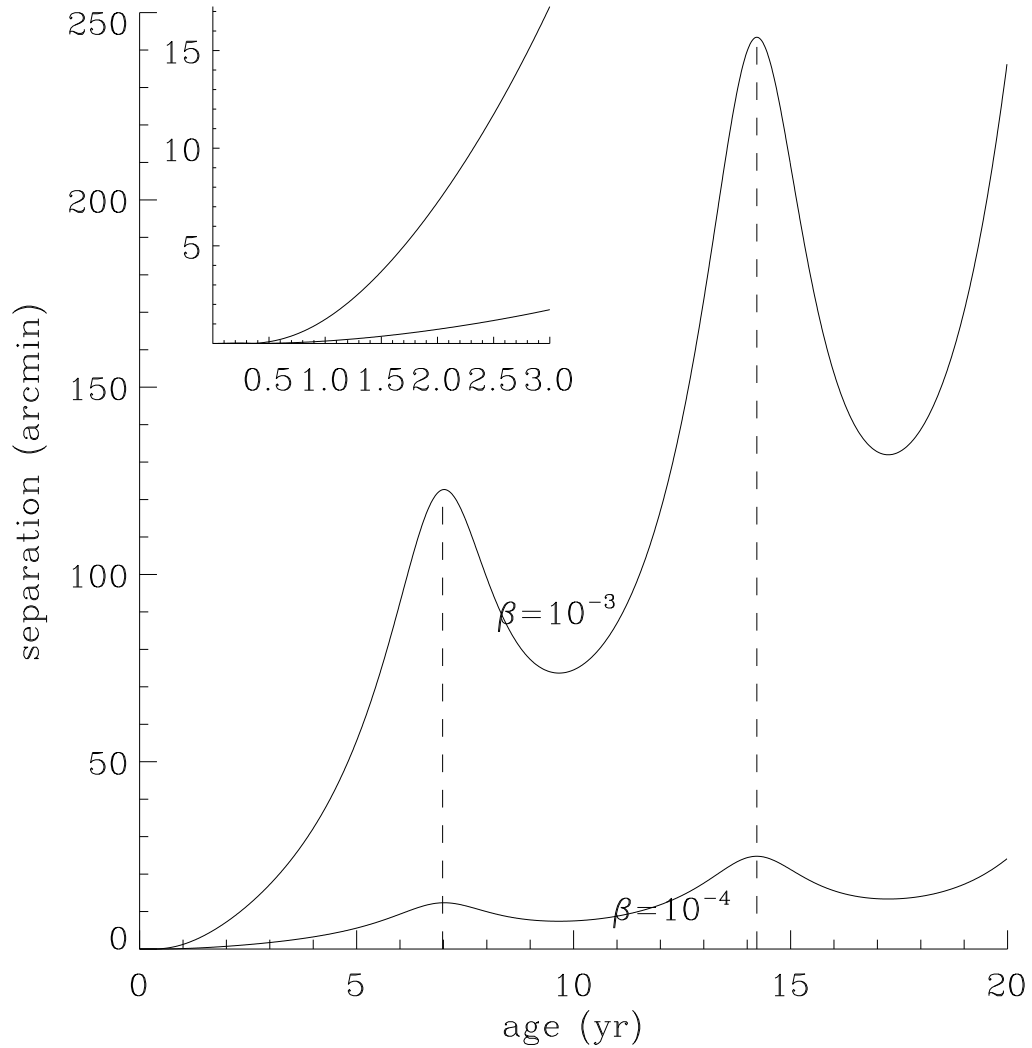


Fig. 9.— The separation of meteoroids from the nucleus as a function of particle age, for 129P/Shoemaker-Levy 3 at the epoch and sky-plane of the *Spitzer* observation in 2005. Dashed lines indicate the ages of particles ejected at each of the previous two perihelion passages. The inset shows the separation versus time for particles younger than 3 yr, at which time zero-ejection-velocity particles with $\beta = 10^{-3}$ would reach the edge of the *Spitzer* image in Figure 7.

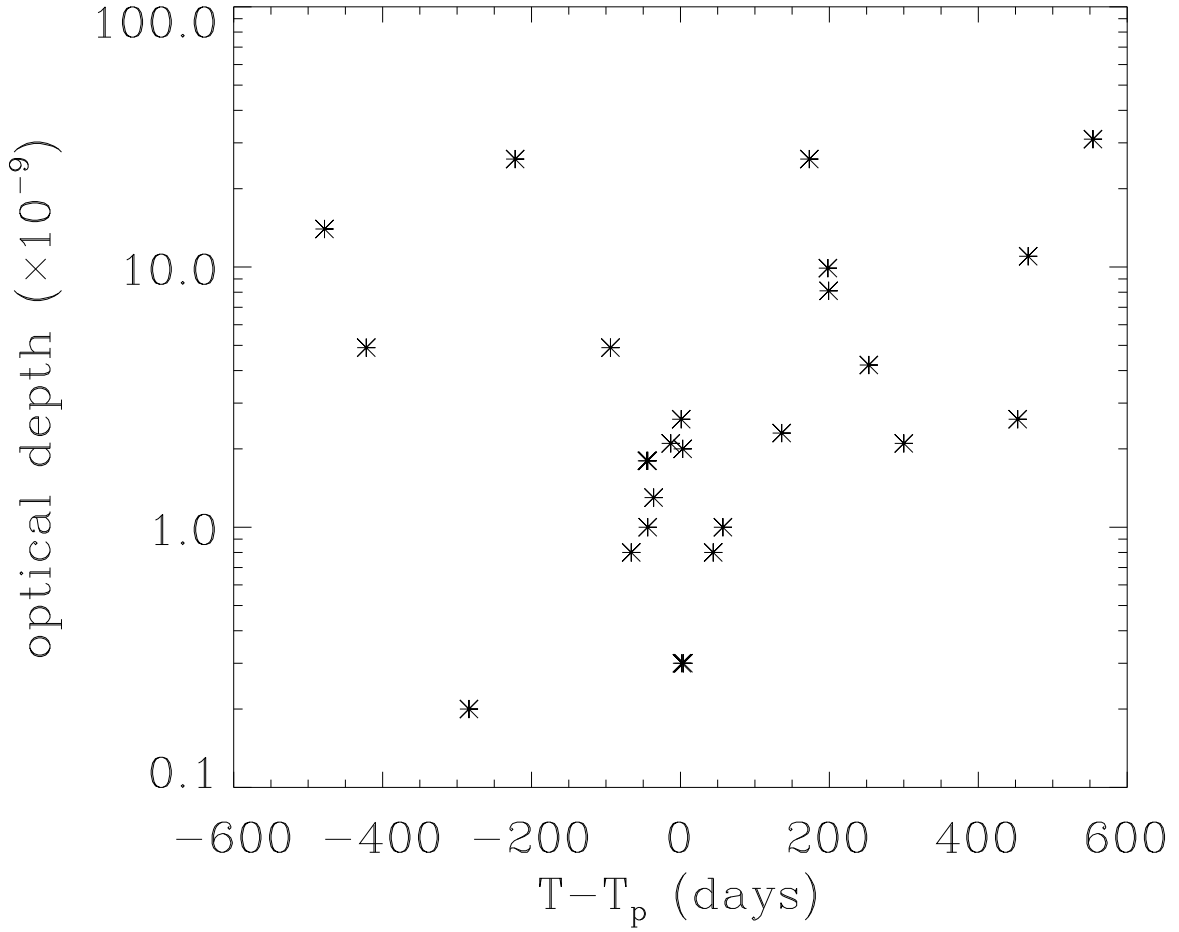


Fig. 10.— Trail optical depth versus the time of observation with respect to the perihelion date, for 30 comets.

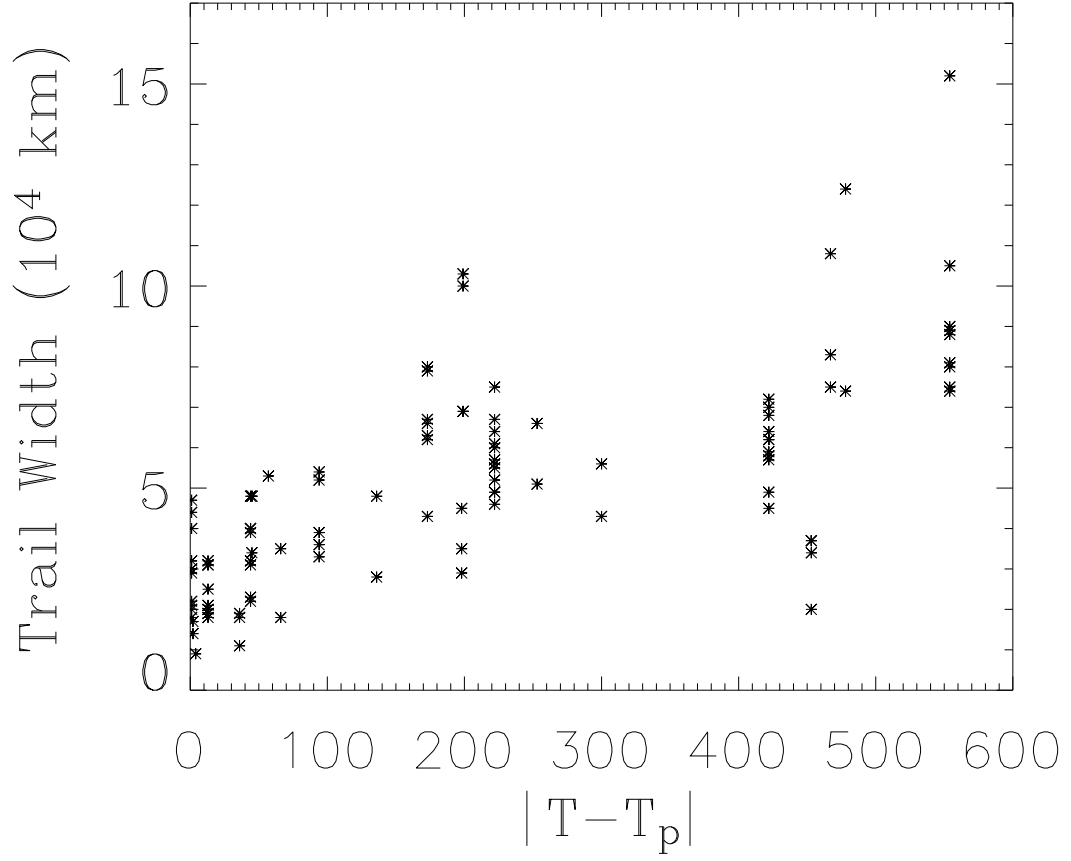


Fig. 12.— Correlation of the debris trail width versus the time of observation relative to perihelion (days).

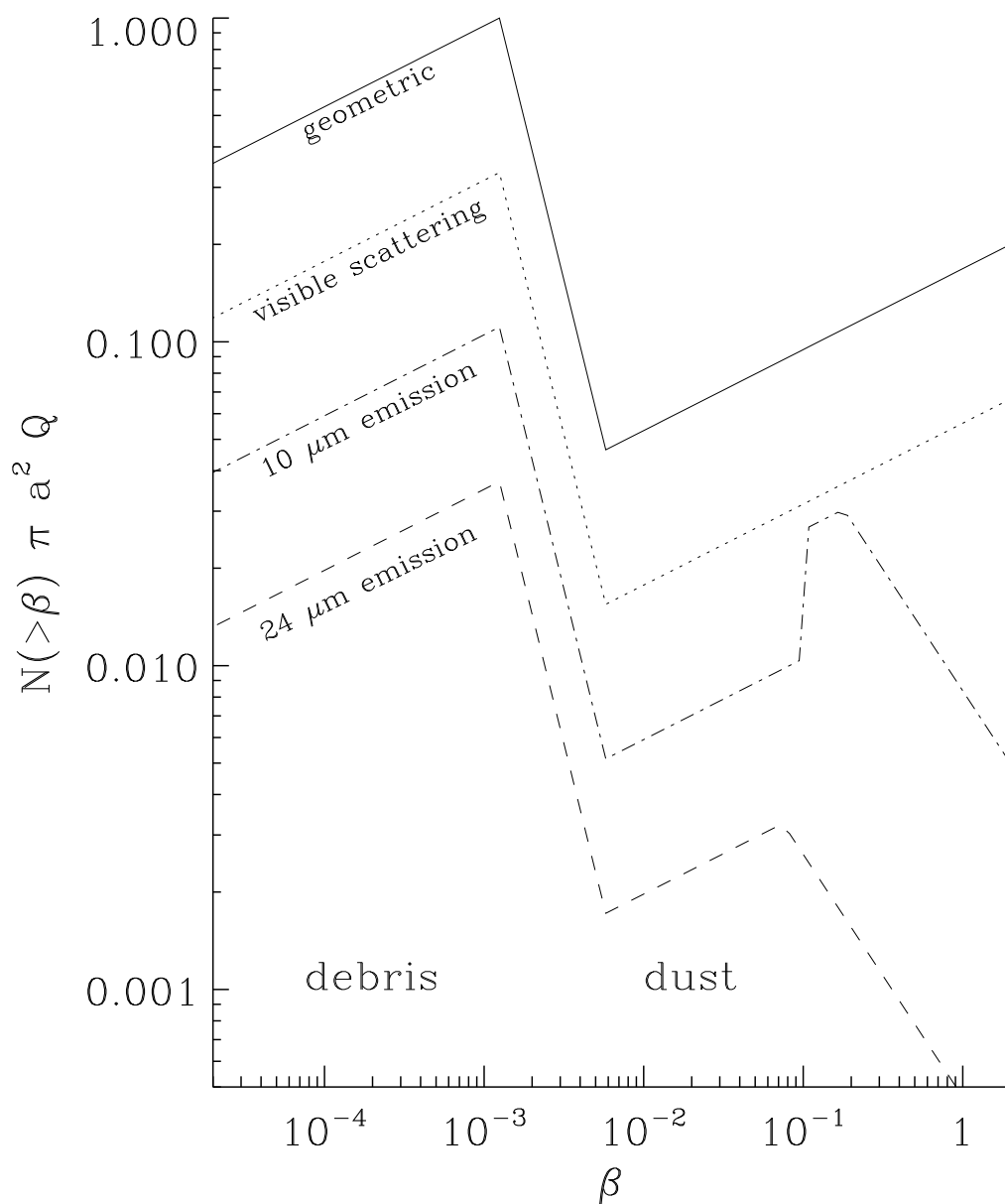


Fig. 13.— Contribution of different sizes to the surface area of cometary particles, for a three-population size distribution similar to that found from the *in situ* observations by dust detectors on the *Stardust* spacecraft in the coma of 81P/Wild 2. Particle sizes on the horizontal axis are parameterized by $\beta/Q_{pr}\rho = 0.57\mu\text{m}/s$, where s is the particle radius, Q_{pr}

is the radiation pressure efficiency in the solar radiation field (~ 1 for particles with $\beta < 0.1$) and ρ is the particle density in g cm^{-3} . The solid line shows the fractional contribution to geometric area; the dotted line shows the contribution to visible light scattering; the dashed line shows the contribution to $24 \mu\text{m}$ emission. The dash-dot line shows the Planck-weighted contribution to $10 \mu\text{m}$ emission (such as the silicate feature), if the smaller grains ($\beta > 0.1$) have higher temperature than the larger grains ($340 \text{ K vs } 280 \text{ K}$). All curves overlap for small β (i.e. on the left side of the plot); then, one by one, each effective cross section diverges from the geometric cross-section, with $24 \mu\text{m}$ emission diverging at lowest β and visible scattering diverging at highest β .